

A Sliced-Wasserstein Framework on Correlation Matrices for EEG Decoding

Chen Hu*
huchen.ml@gmail.com
Westlake University
Hangzhou, China

Rui Wang*
cs_wr@jiangnan.edu.cn
School of Artificial Intelligence and
Computer Science
Jiangnan University
Wuxi, China

Jiale Zhou
zhoujiale@westlake.edu.cn
Westlake University
Hangzhou, China
Zhejiang University
Hangzhou, China

Jingjun Yi
rsjingjuny@whu.edu.cn
Westlake University
Hangzhou, China

Shaocheng Jin
shaochengjin.ai@gmail.com
School of Artificial Intelligence and
Computer Science
Jiangnan University
Wuxi, China

Yidong Song[†]
songyd6@mail2.sysu.edu.cn
Sun Yat-sen University
Guangzhou, China

Yefeng Zheng[†]
zhengyefeng@westlake.edu.cn
Westlake University
Hangzhou, China

Abstract

Electroencephalography (EEG) offers noninvasive, millisecond resolution recordings of neuronal activity and is widely used in neuroscience and healthcare. Many EEG decoding pipelines rely on covariance descriptors for their robustness to noise, but such representations are sensitive to channel-wise scaling. Recent studies have therefore advocated full-rank correlation matrices as a scale-invariant alternative for EEG decoding. In this paper, we propose a general framework for Sliced Wasserstein (SW) discrepancies on manifolds endowed with Pullback Euclidean Metrics (PEMs), termed Pullback Euclidean Metric Sliced Wasserstein (PEMSW). Within this framework, we instantiate two Correlation Sliced-Wasserstein (CorSW) discrepancies on the manifold of full-rank correlation matrices under two recently introduced correlation geometries, *i.e.*, the Off-Log Metric (OLM) and Log-Scaled Metric (LSM). Building on CorSW, we further develop a domain generalization (DG) framework for EEG decoding. Experiments on three EEG datasets demonstrate improved generalization under distribution shifts, with low training overhead and no additional inference cost. The source code is available at github.com/ChenHu-ML/CorSW.

*Equal contribution.

[†]Corresponding authors.

CCS Concepts

• **Applied computing** → **Life and medical sciences**; • **Mathematics of computing** → **Geometric topology**.

Keywords

Electroencephalography (EEG), Neuroscience, Correlation matrices, Sliced-Wasserstein distance, Geometric deep learning

ACM Reference Format:

Chen Hu, Rui Wang, Jiale Zhou, Jingjun Yi, Shaocheng Jin, Yidong Song, and Yefeng Zheng. 2026. A Sliced-Wasserstein Framework on Correlation Matrices for EEG Decoding. In *Proceedings of the 32nd ACM SIGKDD Conference on Knowledge Discovery and Data Mining V.2 (KDD 2026)*, August 9–13, 2026, Jeju Island, Republic of Korea. ACM, New York, NY, USA, 19 pages. <https://doi.org/10.1145/3770855.3818864>

1 Introduction

Electroencephalography (EEG) offers a unique, non-invasive window into brain dynamics by recording neural activity at millisecond time scales. This high temporal resolution has supported a wide spectrum of neuroscience and clinical applications, ranging from seizure detection [2, 28] and sleep staging [1, 68] to motor imagery decoding [3, 48, 72], large-scale abnormality screening [72], affective state analysis [33, 74], and attention tracking in auditory [10]. However, EEG signals are inherently noisy and non-stationary, with statistics that vary substantially across subjects and sessions [42], resulting in pronounced distribution shifts and poor generalization.

A common representation in EEG decoding summarizes the power and spatial distribution of a multi-channel EEG window using covariance matrices [11]. Such matrices are typically symmetric positive definite (SPD) and naturally lie on Riemannian manifolds rather than Euclidean spaces [7]. This has fueled growing interest



This work is licensed under a Creative Commons Attribution 4.0 International License. *KDD 2026, Jeju Island, Republic of Korea.*

© 2026 Copyright held by the owner/author(s).

ACM ISBN 979-8-4007-2259-2/2026/08

<https://doi.org/10.1145/3770855.3818864>

in deep geometric learning, which extends neural networks to non-Euclidean domains by respecting manifold structure. Recent models operate directly on SPD manifolds to leverage their Riemannian geometry [18, 20–27, 44, 45, 78, 79], and SPD-based methods have become competitive baselines for EEG decoding [48, 51, 53, 64].

Nevertheless, covariance-based representations are not always ideal in scientific settings where absolute scales act as nuisance factors. This motivates the use of correlation matrices as normalized and scale-invariant alternatives [34, 75]. Correlation matrices are widely used when relative dependencies matter more than magnitudes, including financial econometrics [71], brain-computer interfaces (BCI) [43, 47], and Gaussian graphical modeling [36]. In EEG analysis, where electrode signal amplitudes often vary substantially, correlation matrices emphasize inter-channel dependencies and remain informative. Despite their importance, correlation matrices have received limited attention in deep geometric learning, as they form a quotient manifold of SPD matrices under the congruence action of positive diagonal matrices [34, 75] and do not admit standard SPD geometry. Only recently have intrinsic Riemannian structures been developed for the correlation manifold, notably the Off-Log Metric (OLM) and Log-Scaled Metric (LSM) [75].

Sets of covariance or correlation matrices extracted from EEG recordings can be naturally viewed as samples from underlying probability distributions [80], motivating the use of distributional comparison tools. This naturally calls for the development of computationally efficient tools that operate directly at the distribution level. In Euclidean spaces, optimal transport (OT) provides a principled framework for comparing probability distributions and induces the Wasserstein distance [67, 77]. OT can be extended to Riemannian manifolds in a way that respects the underlying geometry [31, 49, 60]. However, computing Wasserstein distances typically requires solving large-scale linear programs over the samples, with a computational complexity of $\mathcal{O}(n^3 \log(n))$ in the number of samples n , which becomes prohibitive for large-scale learning.

To alleviate this burden, several alternatives have been proposed, such as entropic regularization [32] or mini-batch approximations [37]. Among them, the Sliced-Wasserstein (SW) distance is particularly appealing, which computes the average Wasserstein distance over one-dimensional projections [69], substantially reducing computational cost while preserving key topological and statistical properties [6, 16, 61]. Building on the success of the Euclidean SW distance, there has been growing interest in generalizing SW to non-Euclidean spaces. Notably, recent works have generalized SW to several classes of vector manifolds, including spherical [12] and hyperbolic spaces [13]. More recently, SW has also been extended to the manifold of SPD matrices [14]. Nevertheless, a principled SW construction tailored to the correlation manifold remains missing.

In this work, we propose a general construction of SW discrepancies on manifolds endowed with Pullback Euclidean Metrics (PEMs), termed PEMS. The key observation is that PEMs arise from global diffeomorphic embeddings, which enable slicing to be defined in a geometrically consistent manner beyond Euclidean spaces. Within this general framework, we derive a concrete instantiation on the manifold of full-rank correlation matrices under two recently introduced correlation geometries, namely OLM and LSM [75], resulting in a practical CorSW discrepancy. Moreover, PEMS provides a unified geometric viewpoint under which existing SW formulations

on SPD manifolds can be recovered as special cases. We finally demonstrate the practical relevance of CorSW by using it to build a domain generalization framework for EEG decoding. In summary, our main contributions are summarized as follows:

- We propose PEMS, a unified construction of SW discrepancies on manifolds endowed with PEMs, which extends classical SW distances to non-Euclidean spaces while preserving intrinsic geometric structure.
- Leveraging PEMS, we instantiate two CorSW discrepancies on the correlation manifold under OLM and LSM.
- We show that existing SPDSW distances on SPD manifolds arise as special cases of PEMS, thereby clarifying the geometric foundations of sliced discrepancies.
- Based on CorSW, we further develop a domain generalization framework for EEG learning and demonstrate its effectiveness across three benchmark EEG datasets, with consistent average gains over correlation-manifold backbones.

2 Preliminary

In this section, we briefly review the PEM, the geometry of full-rank correlation matrices, and the Wasserstein distance. For more in-depth discussions, please refer to [34, 35, 75–77].

Pullback Euclidean metrics. Let \mathcal{M} be a smooth manifold and $(\mathcal{E}, \langle \cdot, \cdot \rangle_{\mathcal{E}})$ denote a finite-dimensional inner-product space. Given a global diffeomorphism $\phi : \mathcal{M} \rightarrow \mathcal{E}$, the PEM on \mathcal{M} is defined as

$$(\phi^* g_{\mathcal{E}})_x(\xi, \eta) \triangleq \langle \phi_{*,x}(\xi), \phi_{*,x}(\eta) \rangle_{\mathcal{E}}, \xi, \eta \in T_x \mathcal{M}, \quad (1)$$

where $\phi_{*,x} : T_x \mathcal{M} \rightarrow T_{\phi(x)} \mathcal{E} \simeq \mathcal{E}$ is the differential at x . In this case, for any $x_0, x_1 \in \mathcal{M}$, the geodesic $\gamma(x_0, x_1, t)$ and the induced distance $d_{\mathcal{M}}(x_0, x_1)$ admit closed-form expressions, given by

$$\gamma(t) = \phi^{-1}((1-t)\phi(x_0) + t\phi(x_1)), \quad (2)$$

$$d_{\mathcal{M}}(x_0, x_1) = \|\phi(x_0) - \phi(x_1)\|_{\mathcal{E}}. \quad (3)$$

Correlation matrices. Given random vector X with invertible covariance matrix $P = (\text{Cov}(X_i, X_j))_{1 \leq i, j \leq n}$, its correlation matrix is defined by variance normalization as

$$C = \text{Cor}(P) = \text{Diag}(P)^{-\frac{1}{2}} P \text{Diag}(P)^{-\frac{1}{2}} \in C_{++}^n, \quad (4)$$

where $\text{Diag}(P)$ denotes the diagonal matrix of P , and C_{++}^n is the set of full-rank correlation matrices. Recent work has shown that C_{++}^n admits several Riemannian metrics induced by diffeomorphisms, which yield closed-form expressions for geodesic distances and curves [75]. In this work, we focus on two metrics: the OLM and the LSM, as summarized in Tab. 1. For OLM, the diffeomorphic pair $(\text{Log}^{\circ}, \text{Exp}^{\circ})$ maps C_{++}^n to $\text{Hol}(n) = \{X \in \mathbb{R}^{n \times n} \mid X = X^{\top}, \text{Diag}(X) = \mathbf{0}\}$, where $\text{Off}(\cdot)$ extracts the off-diagonal part. Following Archakov and Hansen [5, Sec. 3.3], the diagonal correction $\mathcal{D}^{\circ}(S)$ in Exp° is the unique diagonal matrix such that¹

$$\log(\text{Diag}(\exp(S + \mathcal{D}^{\circ}(S)))) = \mathbf{0}. \quad (5)$$

For LSM, $(\text{Log}^{\star}, \text{Exp}^{\star})$ maps C_{++}^n to $\text{Row}_0(n) = \{X \in \mathbb{R}^{n \times n} \mid X = X^{\top}, X\mathbf{1} = \mathbf{0}\}$. The scaling matrix $\mathcal{D}^{\star}(C)$ is defined as the unique positive solution of

$$f : x \in \mathbb{R}^n \mapsto Cx - \frac{1}{x}, \quad (6)$$

¹In implementation, $\mathcal{D}^{\circ}(S)$ is obtained by fixed-point iteration.

Table 1: Summary of diffeomorphic mappings, geodesic distances, and geodesics under OLM and LSM [75].

Metric	Diffeomorphisms	Geodesic Distance $d(C_1, C_2)$	Geodesic from C_1 to $C_2, t \in [0, 1]$
OLM	$\text{Log}^o : C \in C_{++}^n \mapsto \text{Off}(\text{mlog}(C)) \in \text{Hol}(n)$ $\text{Exp}^o : S \in \text{Hol}(n) \mapsto \text{mexp}(S + \mathcal{D}^o(S)) \in C_{++}^n$	$d^o(C_1, C_2) = \ \text{Log}^o(C_1) - \text{Log}^o(C_2)\ _F$	$\text{Exp}^o((1-t)\text{Log}^o(C_1) + t\text{Log}^o(C_2))$
LSM	$\text{Log}^* : C \in C_{++}^n \mapsto \text{mlog}(\mathcal{D}^*(C)C\mathcal{D}^*(C)) \in \text{Row}_0(n)$ $\text{Exp}^* : S \in \text{Row}_0(n) \mapsto \text{Cor}(\text{mexp}(S)) \in C_{++}^n$	$d^*(C_1, C_2) = \ \text{Log}^*(C_1) - \text{Log}^*(C_2)\ _F$	$\text{Exp}^*((1-t)\text{Log}^*(C_1) + t\text{Log}^*(C_2))$

which can be solved using a damped Newton method [75, Sec. 3.5]. In all experiments, we use the standard fixed-point solver for the OLM diagonal correction and damped Newton iterations for the LSM scaling, initialized at the zero diagonal correction and the all-one scaling vector, respectively. These mappings are evaluated once per batch before the one-dimensional SW computations; CorSW therefore requires no iterative OT solver. Consequently, under both OLM and LSM, geodesic distances and geodesics on C_{++}^n admit closed forms as listed in Tab. 1.

Wasserstein distance. Let $\mathcal{P}_p(\mathbb{R}^d)$ be the set of probability measures on \mathbb{R}^d with finite p -th moment for $p \geq 1$. In general, the p -Wasserstein distance between $\mu, \nu \in \mathcal{P}_p(\mathbb{R}^d)$ is defined as

$$W_p^p(\mu, \nu) = \inf_{\gamma \in \Pi(\mu, \nu)} \int_{\mathbb{R}^d \times \mathbb{R}^d} \|x - y\|_2^p d\gamma(x, y), \quad (7)$$

where $\Pi(\mu, \nu)$ is the set of joint distributions with marginals μ and ν . For empirical measures based on n samples, computing W_p requires solving a linear program, whose complexity is $O(n^3 \log n)$ [66], making it impractical for large-scale learning problems.

A key simplification occurs in the one-dimensional case. When $d = 1$, W_p admits an explicit formula [67, Remark 2.30]:

$$W_p^p(\mu, \nu) = \int_0^1 |F_\mu^{-1}(u) - F_\nu^{-1}(u)|^p du, \quad (8)$$

where F_μ^{-1} and F_ν^{-1} denote the quantile functions of μ and ν respectively, which can be computed from n samples in $O(n \log n)$ time. Building on this tractability, the SW distance provides a scalable approximation of W_p in higher dimensions [15, 69]. It is defined by averaging Wasserstein distances between projected measures.

$$\text{SW}_p^p(\mu, \nu) = \int_{S^{d-1}} W_p^p(t_\#^\theta \mu, t_\#^\theta \nu) d\lambda(\theta), \quad (9)$$

where λ is the uniform measure on S^{d-1} . In practice, the integral is approximated via Monte Carlo sampling using L projection directions, resulting in a computational complexity of $O(Ln(d + \log n))$. Beyond computational efficiency, SW_p enjoys strong theoretical guarantees, including dimension-independent sample complexity and a Hilbertian structure [54, 61, 62].

3 Pullback SW Framework

This section presents a pullback SW framework. In Sec. 3.1, we introduce the pullback SW discrepancy PEMSW_p via geodesic slicing and summarize its main theoretical properties. In Sec. 3.2, we instantiate this framework on correlation manifolds C_{++}^n under OLM and LSM, yielding explicit CorSW formulations. In Sec. 3.3, we show that SPDSW arises as a special case of PEMSWS on SPD manifolds. The proofs are deferred to Sec. B.

3.1 Pullback Euclidean SW

In Euclidean spaces, the SW distance is obtained by projecting measures onto one-dimensional lines and averaging the resulting 1D Wasserstein distances. We now generalize this idea to manifolds endowed with PEMs. The key observation is that under PEMs, geodesics become straight lines in the embedding space \mathcal{E} induced by a global diffeomorphism ϕ . As a result, slicing along geodesics on \mathcal{M} reduces to standard linear slicing in \mathcal{E} , leading to a direct analogue of the Euclidean SW construction.

Let $(\mathcal{M}, \phi^*g_{\mathcal{E}})$ be a pullback manifold as in Eq. (3). We fix a reference point $x_0 \in \mathcal{M}$ and write $\langle \cdot, \cdot \rangle_{\mathcal{E}}$ for the Euclidean inner product on \mathcal{E} . Denote by $S_{\mathcal{E}} = \{a \in \mathcal{E} : \|a\|_{\mathcal{E}} = 1\}$ the unit sphere in \mathcal{E} , equipped with the uniform measure $\lambda_{\mathcal{E}}$.

Geodesic slicing. We consider geodesics through the reference point x_0 , and use the corresponding signed scalar coordinate as a one-dimensional projection. For a direction $a \in S_{\mathcal{E}}$, the pullback Euclidean structure maps geodesics on \mathcal{M} to straight lines in the embedding space \mathcal{E} , which gives the explicit geodesic line

$$\mathcal{G}_a = \left\{ \phi^{-1}(\phi(x_0) + ta) : t \in \mathbb{R} \right\}. \quad (10)$$

The slicing coordinate of $x \in \mathcal{M}$ is obtained by $\phi(x)$ onto the direction $a \in S_{\mathcal{E}}$, which yields the closed-form expressions in Thm. 3.1.

Theorem 3.1 (Projection and slicing coordinate on PEMs). *Let $a \in S_{\mathcal{E}}$. For any $x \in \mathcal{M}$, the projection of x onto \mathcal{G}_a admits the form*

$$p^{\mathcal{G}_a}(x) = \phi^{-1}(\phi(x_0) + t_a(x)a) \in \mathcal{G}_a, \quad (11)$$

where the associated slicing coordinate is

$$t_a(x) = \langle a, \phi(x) - \phi(x_0) \rangle_{\mathcal{E}}. \quad (12)$$

PEMSW discrepancy. We now define the PEMSWS discrepancy. For $p \geq 1$, define the p -moment class on $(\mathcal{M}, d_{\mathcal{M}})$ by

$$\mathcal{P}_p(\mathcal{M}) = \left\{ \mu \in \mathcal{P}(\mathcal{M}) : \int_{\mathcal{M}} d_{\mathcal{M}}(x, x_0)^p d\mu(x) < \infty \right\}. \quad (13)$$

We then average one-dimensional Wasserstein distances between the push-forward measures of slicing coordinates Eq. (12) over random directions $a \in S_{\mathcal{E}}$.

Definition 3.2 (PEMSWS). Let $p \geq 1$ and $\mu, \nu \in \mathcal{P}_p(\mathcal{M})$. The SW under PEM discrepancy is

$$\text{PEMSW}_p(\mu, \nu)^p = \int_{S_{\mathcal{E}}} W_p^p(t_{a\#}\mu, t_{a\#}\nu) d\lambda_{\mathcal{E}}(a). \quad (14)$$

In practice, the integral in Eq. (14) is approximated by Monte Carlo sampling, and each one-dimensional W_p is computed via order statistics. More importantly, the pullback structure $g = \phi^*g_{\mathcal{E}}$ allows us to work directly in the embedding space \mathcal{E} . The slicing

coordinate t_a admits a linear form in $\phi(x)$ up to a constant shift. Lem. 3.3 links PEMSW_p and W_p^M to their Euclidean counterparts between the embedded measures $\tilde{\mu} = \phi_{\#}\mu$ and $\tilde{\nu} = \phi_{\#}\nu$.

Lemma 3.3 (Translation form of t_a). *For $a \in S_{\mathcal{E}}$, define $\pi_a : \mathcal{E} \rightarrow \mathbb{R}$ by $\pi_a(z) = \langle a, z \rangle_{\mathcal{E}}$. Then for all $x \in \mathcal{M}$,*

$$t_a(x) = \pi_a(\phi(x)) - \pi_a(\phi(x_0)). \quad (15)$$

Consequently, $t_{a\#}\mu$ is a translation of $\pi_{a\#}\tilde{\mu}$, and the same holds for ν .

Using the translation invariance of the one-dimensional Wasserstein distance, we obtain the following equivalence in Thm. 3.4.

Theorem 3.4 (Equivalence to Euclidean SW). *For any $p \geq 1$ and $\mu, \nu \in \mathcal{P}_p(\mathcal{M})$, PEMSW_p and W_p^M can be evaluated in the embedding space \mathcal{E} via $\tilde{\mu} = \phi_{\#}\mu$ and $\tilde{\nu} = \phi_{\#}\nu$:*

$$\text{PEMSW}_p(\mu, \nu) = \text{SW}_p(\tilde{\mu}, \tilde{\nu}), \quad W_p^M(\mu, \nu) = W_p(\tilde{\mu}, \tilde{\nu}). \quad (16)$$

Thm. 3.4 shows that PEMSW_p is exactly the Euclidean SW distance between the embedded measures. Since the slicing coordinate t_a is defined relative to a reference point x_0 , we next show that PEMSW_p is in fact independent of this choice.

Proposition 3.5 (Reference-point invariance). *Let $p \geq 1$ and $x_0, x_1 \in \mathcal{M}$. For $a \in S_{\mathcal{E}}$, the slicing coordinates associated with x_0 and x_1 are defined as*

$$t_a^{(x_i)}(x) = \langle a, \phi(x) - \phi(x_i) \rangle_{\mathcal{E}}, \quad i \in \{0, 1\}. \quad (17)$$

Then for all $\mu, \nu \in \mathcal{P}_p(\mathcal{M})$,

$$W_p(t_a^{(x_0)\#}\mu, t_a^{(x_0)\#}\nu) = W_p(t_a^{(x_1)\#}\mu, t_a^{(x_1)\#}\nu), \quad \forall a \in S_{\mathcal{E}}. \quad (18)$$

Hence, PEMSW_p is invariant to the choice of the reference point.

Theoretical properties. The PEMSW_p inherits fundamental properties from the one-dimensional and Euclidean SW distances. We summarize below its metric, topological, and comparison properties, which justify PEMSW_p as a computationally tractable surrogate of the Wasserstein distance on \mathcal{M} .

Theorem 3.6 (Metric structure of PEMSW_p). *For $p \geq 1$ and $\mu, \nu \in \mathcal{P}_p(\mathcal{M})$, the quantity $\text{PEMSW}_p(\mu, \nu)$ defines a finite distance on $\mathcal{P}_p(\mathcal{M})$. In particular, it is symmetric, satisfies the triangle inequality, and vanishes if and only if $\mu = \nu$.*

PEMSW_p also induces the same weak topology as the Euclidean Wasserstein distance.

Theorem 3.7 (Weak convergence). *Let $p \geq 1$ and $\mu \in \mathcal{P}_p(\mathcal{M})$. For any sequence $(\mu_k)_k \subset \mathcal{P}_p(\mathcal{M})$,*

$$\mu_k \rightharpoonup \mu \quad \text{if and only if} \quad \text{PEMSW}_p(\mu_k, \mu) \rightarrow 0. \quad (19)$$

We next relate PEMSW_p to the Wasserstein distance W_p^M through a set of comparison inequalities. These results clarify the approximation behavior of PEMSW_p with respect to W_p^M .

Proposition 3.8 (Upper bound comparison to W_p^M). *For $p \geq 1$ and $\mu, \nu \in \mathcal{P}_p(\mathcal{M})$,*

$$\text{PEMSW}_p(\mu, \nu)^p \leq \kappa_{D,p} W_p^M(\mu, \nu)^p, \quad (20)$$

where $D = \dim(\mathcal{E})$ and $\kappa_{D,p} = \int_{S^{D-1}} |\theta_1|^p d\lambda(\theta)$. Specifically, when $p = 2$, $\kappa_{D,2} = 1/D$ and $\text{PEMSW}_2(\mu, \nu)^2 \leq \frac{1}{D} W_2^M(\mu, \nu)^2$.

We then provide a complementary lower bound highlighting the sensitivity of PEMSW_p to discrepancies in first-order moments.

Proposition 3.9 (Moment lower bound). *For $\mu, \nu \in \mathcal{P}_p(\mathcal{M})$ with finite first moments of their embeddings $\tilde{\mu} = \phi_{\#}\mu$ and $\tilde{\nu} = \phi_{\#}\nu$ in \mathcal{E} ,*

$$\text{PEMSW}_p(\mu, \nu)^p \geq \int_{S_{\mathcal{E}}} |\langle a, m_{\tilde{\mu}} - m_{\tilde{\nu}} \rangle_{\mathcal{E}}|^p d\lambda_{\mathcal{E}}(a) = \kappa_{D,p} \|m_{\tilde{\mu}} - m_{\tilde{\nu}}\|_{\mathcal{E}}^p, \quad (21)$$

where $D = \dim(\mathcal{E})$ and $\kappa_{D,p} = \int_{S^{D-1}} |\theta_1|^p d\lambda(\theta)$.

A max-sliced formulation further provides a tighter, albeit more expensive, alternative.

Proposition 3.10 (Max-sliced formulation). *The max-sliced discrepancy can be defined by*

$$\text{PEM-MaxSW}_p(\mu, \nu) = \sup_{a \in S_{\mathcal{E}}} W_p(t_{a\#}\mu, t_{a\#}\nu). \quad (22)$$

Then, for all $\mu, \nu \in \mathcal{P}_p(\mathcal{M})$,

$$\text{PEMSW}_p(\mu, \nu) \leq \text{PEM-MaxSW}_p(\mu, \nu) \leq W_p^M(\mu, \nu). \quad (23)$$

Finally, on compactly supported measures, PEMSW_p also controls W_p^M from below via a reverse inequality.

Theorem 3.11 (Compact-support reverse bound). *Let $p \geq 1$ and fix $R > 0$. Define the Euclidean ball in \mathcal{E} by*

$$B_{\mathcal{E}}(\phi(x_0), R) = \{z \in \mathcal{E} : \|z - \phi(x_0)\|_{\mathcal{E}} \leq R\}, \quad (24)$$

and its pullback subset $\mathcal{M}_R = \phi^{-1}(B_{\mathcal{E}}(\phi(x_0), R))$. Then there exists a constant $C_{D,p,R} > 0$ such that for all $\mu, \nu \in \mathcal{P}_p(\mathcal{M}_R)$,

$$W_p^M(\mu, \nu)^p \leq C_{D,p,R} \text{PEMSW}_p(\mu, \nu)^{\frac{1}{D+1}}. \quad (25)$$

Statistical properties. In practice, we approximate PEMSW_p using (i) plug-in empirical measures and (ii) a Monte-Carlo estimate of the outer integral. We provide below generic bounds for both sources of error.

Proposition 3.12 (Plug-in stability under pullback slicing). *Let $q > p \geq 1$ and $\mu, \nu \in \mathcal{P}_q(\mathcal{M})$, with empirical measures $\hat{\mu}_n$ and $\hat{\nu}_n$ constructed from i.i.d. samples. Denote by $\tilde{\mu} = \phi_{\#}\mu$ and $\tilde{\nu} = \phi_{\#}\nu$ the corresponding embedded measures in \mathcal{E} , and quantify their tail behavior through the q -th order moments*

$$M_q(\tilde{\mu}) = \int_{\mathcal{E}} \|z - \phi(x_0)\|_{\mathcal{E}}^q d\tilde{\mu}(z), \quad (26)$$

$$M_q(\tilde{\mu}, \tilde{\nu}) = M_q(\tilde{\mu})^{1/q} + M_q(\tilde{\nu})^{1/q}. \quad (27)$$

There exists a constant $C_{p,q}$, depending only on p and q , such that

$$\mathbb{E} \left[\left| \text{PEMSW}_p(\hat{\mu}_n, \hat{\nu}_n) - \text{PEMSW}_p(\mu, \nu) \right| \right] \leq \alpha_{n,p,q} C_{p,q}^{1/p} M_q(\tilde{\mu}, \tilde{\nu}), \quad (28)$$

$$\alpha_{n,p,q} = \begin{cases} n^{-1/(2p)} & \text{if } q > 2p, \\ n^{-1/(2p)} \log(n)^{1/p} & \text{if } q = 2p, \\ n^{-(q-p)/(pq)} & \text{if } q \in (p, 2p). \end{cases} \quad (29)$$

Proposition 3.13 (Monte-Carlo approximation under random pullback directions). *Let $p \geq 1$ and $\mu, \nu \in \mathcal{P}_p(\mathcal{M})$. Consider L independent slicing directions $(a_i)_{i=1}^L$ drawn uniformly from the unit sphere*

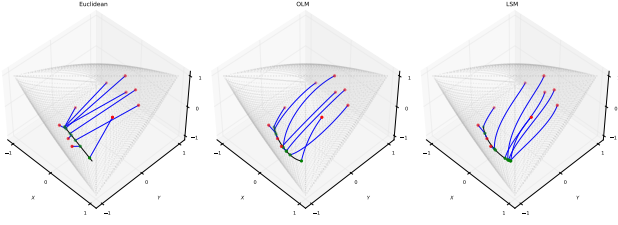


Figure 1: Visualization of Euclidean projections (left) and geodesic projections under OLM (middle) and LSM (right) for 3×3 correlation matrices.

$S_{\mathcal{E}}$ of the embedding space. The empirical approximation of PEMSW_p based on these directions is given by

$$\widehat{\text{PEMSW}}_{p,L}^p(\mu, \nu) = \frac{1}{L} \sum_{i=1}^L W_p^p(t_{a_i \# \mu}, t_{a_i \# \nu}). \quad (30)$$

The error induced by random sampling of pullback slicing directions admits the bound

$$\begin{aligned} \mathbb{E} \left[\left| \widehat{\text{PEMSW}}_{p,L}^p(\mu, \nu) - \text{PEMSW}_p^p(\mu, \nu) \right|^2 \right] \\ \leq \frac{1}{L} \text{Var}_{a \sim \lambda_{\mathcal{E}}} \left[W_p^p(t_{a \# \mu}, t_{a \# \nu}) \right]. \end{aligned} \quad (31)$$

3.2 Correlation SW

We now specialize the general PEMS W construction to correlation manifolds C_{++}^n endowed with OLM and LSM as shown in Tab. 1. In both cases, the associated embedding space \mathcal{E} is a linear subspace equipped with the Frobenius inner product $\langle A, B \rangle_F = \text{Tr}(A^\top B)$. To provide geometric intuition, Fig. 1 visualizes geodesic projections of a 3×3 correlation matrix under OLM and LSM metrics, together with Euclidean projections, illustrating how different geometries induce distinct projection behaviors on correlation manifolds.

OLM. Under the OLM, we take $\phi = \text{Log}^o : C_{++}^n \rightarrow \text{Hol}(n)$ with embedding space $\mathcal{E} = \text{Hol}(n)$. Since $\text{Log}^o(I_n) = 0$, we fix the reference point as $x_0 = I_n$. The general geodesic slicing construction in Thm. 3.1 then admits the following explicit form.

Corollary 3.14 (Geodesic projection under OLM). *Let $\mathcal{M} = C_{++}^n$, $\phi = \text{Log}^o$, and $x_0 = I_n$. For any direction $A \in S_{\text{Hol}}$ and any $C \in C_{++}^n$, the corresponding slicing coordinate is given by*

$$t_A^o(C) = \langle A, \text{Log}^o(C) \rangle_F. \quad (32)$$

This leads naturally to the definition of an SW discrepancy on C_{++}^n induced by the OLM geometry.

Definition 3.15 (CorSW under OLM). Let $p \geq 1$ and $\mu, \nu \in \mathcal{P}_p(C_{++}^n)$. The correlation SW distance under OLM is defined as

$$\text{CorSW}_p^o(\mu, \nu)^p = \int_{S_{\text{Hol}}} W_p^p(t_{A \# \mu}^o, t_{A \# \nu}^o) d\lambda_{\text{Hol}}(A), \quad (33)$$

where $S_{\text{Hol}} = \{A \in \text{Hol}(n) : \|A\|_F = 1\}$ is endowed with the uniform measure λ_{Hol} .

LSM. Similarly, under the LSM we take $\phi = \text{Log}^* : C_{++}^n \rightarrow \text{Row}_0(n)$ with embedding space $\mathcal{E} = \text{Row}_0(n)$, and again fix $x_0 = I_n$. In this case, the geodesic slicing coordinate takes the following form.

Corollary 3.16 (Geodesic projection under LSM). *Let $\mathcal{M} = C_{++}^n$, $\phi = \text{Log}^*$, and $x_0 = I_n$. For any direction $A \in S_{\text{Row}}$ and any $C \in C_{++}^n$, the slicing coordinate is given by*

$$t_A^*(C) = \langle A, \text{Log}^*(C) \rangle_F. \quad (34)$$

The SW discrepancy induced by LSM is defined as follows.

Definition 3.17 (CorSW under LSM). Let $p \geq 1$ and $\mu, \nu \in \mathcal{P}_p(C_{++}^n)$. The correlation SW distance under LSM is defined by

$$\text{CorSW}_p^*(\mu, \nu)^p = \int_{S_{\text{Row}}} W_p^p(t_{A \# \mu}^*, t_{A \# \nu}^*) d\lambda_{\text{Row}}(A), \quad (35)$$

where $S_{\text{Row}_0} = \{A \in \text{Row}_0(n) : \|A\|_F = 1\}$ is endowed with the uniform measure λ_{Row} .

3.3 SPDSW as a Special Case of PEMS W

Bonet et al. [14] proposed the SPDSW distance on SPD manifolds by applying a matrix logarithm embedding followed by random one-dimensional linear projections. In this section, we show that SPDSW arises as a special case of the proposed PEMS W framework. Specifically, when $\mathcal{M} = S_d^{++}$ and the embedding map ϕ is chosen as the matrix logarithm, the induced geodesics correspond to straight lines in the space of symmetric matrices, and the resulting slicing coordinates coincide with those of SPDSW. Moreover, the slicing distribution used in SPDSW, constructed via Haar-distributed orthogonal bases and uniformly sampled eigenvalue directions, induces the uniform distribution on the unit Frobenius sphere of symmetric matrices [14, Lem. 2.4]. This is fully consistent with the uniform slicing assumption in PEMS W .

Proposition 3.18 (SPDSW as an instance of PEMS W). *Let $\mathcal{M} = S_d^{++}$ and let ϕ be a matrix logarithm embedding defining a pullback Euclidean metric on \mathcal{M} . Then the PEMS W discrepancy reduces exactly to the SPDSW distance, namely*

$$\text{PEMSW}_p(\mu, \nu) = \text{SPDSW}_p(\mu, \nu), \quad \forall \mu, \nu \in \mathcal{P}_p(S_d^{++}). \quad (36)$$

From this perspective, SPDSW is recovered as a particular realization of PEMS W on SPD manifolds. The PEMS W framework, therefore, provides a unifying geometric viewpoint that not only recovers existing SW constructions on SPD manifolds but also extends them naturally to broader manifolds endowed with PEMS.

4 Experiments

In this section, we evaluate the proposed CorSW framework across three EEG decoding paradigms, examining its predictive performance, robustness to cross-session domain shifts, key design choices, training efficiency, and neurophysiological interpretability.

4.1 Domain Generalization with CorSW

We adopt CorSW as a source-only domain generalization (DG) objective by aligning correlation representations of each source domain to a common reference law. For a source domain d , let $C^d \subset C_{++}^n$ denote the empirical distribution of its feature-level correlation matrices. Rather than matching all source domains pairwise, CorSW

Algorithm 1: Correlation SW domain generalization loss

Input: batch $\mathcal{B} = \{C_i \in C_{++}^n, d(i) \in \mathcal{D}_{\mathcal{B}}\}_{i=1}^M; g \in \{o, \star\};$
number of slices S ; order $p = 2$

Initialize $\mathcal{L}_{\text{swd}} \leftarrow 0$

for each domain $d \in \mathcal{D}_{\mathcal{B}}$ **do**

$C^d \leftarrow \{C_i \mid d(i) = d\}$

$\bar{Z}^d \sim \mathcal{N}(0, I)$ with $\text{shape}(C^d)$

$Z^d \leftarrow \Pi_{\mathcal{E}_g}(\bar{Z}^d)$ // Project to \mathcal{E}_g

$Q^d \leftarrow \text{Exp}^g\left(\frac{Z^d}{\|Z^d\|_{\text{F}} + \epsilon}\right) \subset C_{++}^n$ // Reference distribution

Initialize $\ell^d \leftarrow 0$

for $s = 1$ **to** S **do**

$A_s \sim \text{Unif}(\mathbb{S}_{\mathcal{E}})$ // Uniform unit slicing direction

$u_s^d \leftarrow t_{A_s}^g(C^d), v_s^d \leftarrow t_{A_s}^g(Q^d)$ // 1D slicing along A_s

$\ell^d \leftarrow \ell^d + W_p^p(u_s^d, v_s^d)$

end

$\mathcal{L}_{\text{swd}} \leftarrow \mathcal{L}_{\text{swd}} + \ell^d / S$

end

return \mathcal{L}_{swd}

aligns each C^d to the same domain-agnostic reference law, which avoids selecting a particular source as the alignment target and keeps the loss linear in the number of source domains.

The reference samples are generated in the geometry-specific embedding subspace \mathcal{E}_g , with $\mathcal{E}_o = \text{Hol}(n)$ for OLM and $\mathcal{E}_{\star} = \text{Row}_0(n)$ for LSM. Specifically, Gaussian matrix samples are first projected onto \mathcal{E}_g and then mapped back to C_{++}^n through Exp^g , ensuring valid inputs for the selected geometry. In each mini-batch, an independent reference set Q^d with the same cardinality as C^d is sampled for stable one-dimensional Wasserstein matching. The discrepancy between C^d and Q^d is measured by CorSW through random geodesic slicing. For each direction $A_s \sim \text{Unif}(\mathbb{S}_{\mathcal{E}_g})$, both distributions are projected by $t_{A_s}^g$ and compared using the p -Wasserstein distance. The final loss averages over slicing directions and sums across source domains, encouraging domain-invariant representations while preserving correlation-manifold geometry. The overall procedure is summarized in Alg. 1.

4.2 Datasets and Preprocessing

We conduct experiments on three representative BCI paradigms that cover both time-asynchronous and time-synchronous EEG decoding scenarios, each exhibiting distinct neurophysiological characteristics. Specifically, we evaluate motor imagery (MI) decoding on the BCIC-IV-2a dataset [19], which represents a typical time-asynchronous setting, and steady-state visual evoked potential (SSVEP) decoding on the MAMEM-SSVEP-II dataset [63] as well as error-related negativity (ERN) decoding on the BCI-ERN dataset [59], both of which correspond to time-synchronous EEG paradigms. This diverse experimental setup allows us to comprehensively assess the effectiveness and generality of the proposed method across different temporal structures and decoding regimes.

MI. The BCIC-IV-2a dataset [19] is a widely used benchmark for MI decoding. It consists of EEG recordings from nine subjects performing four-class MI tasks, namely left hand, right hand, feet,

Table 2: Average task performance (\pm std., %) over 10 runs for baseline and CorAtt models with and without CorSW.

Models	MI	SSVEP	ERN
<i>Euclidean methods</i>			
EEGNet [55]	61.84 \pm 6.39	53.72 \pm 7.23	74.28 \pm 2.47
ShallowCNet [73]	57.43 \pm 6.25	56.93 \pm 6.97	71.86 \pm 2.64
EEG-TCNet [46]	67.09 \pm 4.66	55.45 \pm 7.66	77.05 \pm 2.46
FBCNet [58]	56.52 \pm 3.07	53.09 \pm 5.67	60.47 \pm 3.06
MBEEGSE [4]	64.58 \pm 6.07	56.45 \pm 7.27	75.46 \pm 2.34
<i>Riemannian methods</i>			
MAtt [64]	74.71 \pm 5.01	65.19 \pm 3.14	75.68 \pm 2.23
GDLNet [78]	69.32 \pm 2.89	65.52 \pm 2.86	78.23 \pm 2.52
CorAtt-OLM [43]	75.01 \pm 2.78	67.39 \pm 3.22	78.78 \pm 3.40
CorAtt-OLM+CorSW-OLM (Ours)	75.49 \pm 2.34	68.58 \pm 1.01	81.33 \pm 1.14
CorAtt-LSM [43]	74.47 \pm 2.43	67.74 \pm 2.44	78.63 \pm 3.31
CorAtt-LSM+CorSW-LSM (Ours)	74.98 \pm 2.67	68.60 \pm 1.62	80.07 \pm 0.89
CorAtt-MIX [43]	75.56 \pm 1.58	68.27 \pm 2.50	79.04 \pm 2.91
CorAtt-MIX+CorSW-OLM (Ours)	75.58 \pm 1.23	68.51 \pm 1.30	79.90 \pm 2.44

and tongue movements. Each subject participated in two recording sessions, and each trial has a duration of four seconds. Classification accuracy is used as the evaluation metric.

SSVEP. The MAMEM-SSVEP-II dataset [63] contains EEG recordings from eleven subjects, each recorded over five sessions. In each session, subjects were instructed to visually attend to flickering stimuli at five target frequencies (6.66, 7.50, 8.57, 10.00, and 12.00 Hz), yielding one trial per frequency. We use the 1–5 second interval after stimulus onset and split each trial into four non-overlapping one-second segments for model input. This produces 20 input segments per session and 100 segments per subject across all sessions. Classification accuracy is used as the evaluation metric.

ERN. The BCI-ERN dataset [59] originates from a Kaggle BCI Challenge and includes EEG recordings from 26 participants engaged in a P300-based spelling task. ERN signals are elicited following incorrect feedback, leading to a binary classification problem with a pronounced class imbalance. To account for this imbalance, performance is evaluated using the area under the receiver operating characteristic curve (AUC).

4.3 Experimental Setup

A major challenge in EEG decoding is the pronounced domain shift across subjects and sessions, which often leads to performance degradation. This challenge motivates the use of DG techniques that aim to learn domain-invariant representations without access to target-domain data. In our experiments, we adopt CorAtt [43] as the correlation-manifold backbone and evaluate the proposed CorSW-based DG objective under three geometric instantiations: CorAtt-OLM, CorAtt-LSM, and CorAtt-MIX. CorAtt-OLM and CorAtt-LSM use a single correlation geometry throughout the network, based on the OLM and LSM, respectively, while CorAtt-MIX combines OLM in the attention module with LSM in the classification layer. CorSW is applied to the correlation representations produced by the attention module, where distribution shifts are first expressed on the correlation manifold. Accordingly, the geometry used by CorSW is chosen to match the representation space on which the loss is imposed: OLM for CorAtt-OLM and CorAtt-MIX, and LSM for

Table 3: Cross-session DG results (%) on MI, SSVEP, and ERN tasks.

Models	MI		SSVEP					ERN					Mean
	S1→S2	S2→S1	S1234→S5	S2345→S1	S1345→S2	S1245→S3	S1235→S4	S1234→S5	S2345→S1	S1345→S2	S1245→S3	S1235→S4	
CorAtt-OLM	70.53 ± 2.12	74.71 ± 2.40	67.13 ± 0.67	66.55 ± 1.05	66.34 ± 0.76	67.94 ± 0.79	69.79 ± 0.85	76.67 ± 0.44	79.73 ± 0.91	81.77 ± 0.82	80.56 ± 0.36	81.07 ± 0.53	73.57
+ IW [29]	70.85 ± 2.44	74.95 ± 2.06	67.58 ± 0.71	67.02 ± 1.30	67.05 ± 0.68	68.51 ± 1.01	68.00 ± 0.87	77.35 ± 0.37	82.44 ± 1.09	84.61 ± 0.73	83.50 ± 0.37	83.73 ± 0.64	74.63
+ DAC-SC [56]	69.86 ± 2.54	74.18 ± 2.25	66.39 ± 0.71	65.96 ± 0.92	65.83 ± 0.89	67.67 ± 0.94	69.43 ± 0.90	76.00 ± 0.48	81.58 ± 0.95	83.36 ± 0.91	81.66 ± 0.45	82.61 ± 0.66	73.71
+ RIW [56]	70.64 ± 2.42	74.91 ± 2.36	67.34 ± 0.75	66.83 ± 1.15	66.60 ± 0.67	68.11 ± 0.98	68.76 ± 0.75	76.75 ± 0.50	82.25 ± 1.02	84.37 ± 0.80	83.16 ± 0.43	83.65 ± 0.56	74.45
+ DRIW [9]	70.96 ± 2.55	75.01 ± 2.25	67.64 ± 0.76	67.04 ± 1.07	66.82 ± 0.83	68.42 ± 0.99	69.44 ± 0.75	77.15 ± 0.54	82.44 ± 0.94	84.66 ± 0.83	83.50 ± 0.44	83.86 ± 0.59	74.75
+ CorSW-OLM (Ours)	71.31 ± 2.26	75.49 ± 2.34	68.58 ± 1.01	68.51 ± 1.00	70.26 ± 1.05	71.49 ± 0.75	69.05 ± 1.77	81.33 ± 1.14	82.49 ± 2.67	85.03 ± 0.41	84.55 ± 0.25	84.11 ± 0.87	76.02
	+0.78	+0.78	+1.45	+1.96	+3.92	+3.55	-0.74	+4.66	+2.76	+3.26	+3.99	+3.04	+2.45
CorAtt-LSM	69.72 ± 2.42	73.46 ± 2.15	67.52 ± 1.30	66.88 ± 0.96	66.91 ± 1.05	68.35 ± 0.52	69.89 ± 1.02	76.49 ± 0.82	79.35 ± 0.61	82.26 ± 0.36	80.40 ± 0.28	80.47 ± 0.61	73.47
+ IW [29]	70.08 ± 2.28	73.85 ± 2.19	67.81 ± 1.20	67.11 ± 1.02	67.12 ± 1.12	68.67 ± 0.46	70.31 ± 1.12	76.94 ± 0.90	82.06 ± 0.55	84.84 ± 0.40	82.95 ± 0.31	83.12 ± 0.55	74.57
+ DAC-SC [56]	69.01 ± 2.67	72.96 ± 2.01	66.87 ± 1.37	66.07 ± 1.09	66.28 ± 1.06	67.65 ± 0.53	69.29 ± 0.96	75.69 ± 0.79	81.22 ± 0.57	84.03 ± 0.31	82.20 ± 0.28	82.29 ± 0.55	73.63
+ RIW [56]	69.94 ± 2.66	73.69 ± 2.12	67.71 ± 1.28	67.05 ± 0.98	67.09 ± 1.21	68.55 ± 0.53	70.19 ± 0.95	76.83 ± 0.90	81.96 ± 0.58	84.79 ± 0.36	82.88 ± 0.33	83.06 ± 0.64	74.48
+ DRIW [9]	70.03 ± 2.18	74.01 ± 2.30	67.99 ± 1.33	67.28 ± 1.04	67.33 ± 0.97	68.88 ± 0.45	70.53 ± 1.07	77.18 ± 0.94	82.17 ± 0.66	85.03 ± 0.38	83.12 ± 0.29	83.29 ± 0.70	74.74
+ CorSW-LSM (Ours)	70.23 ± 2.87	74.98 ± 2.67	68.60 ± 1.62	68.54 ± 0.66	69.48 ± 1.19	72.23 ± 0.27	68.16 ± 0.99	80.07 ± 0.89	82.07 ± 2.04	85.71 ± 0.88	84.31 ± 1.27	83.36 ± 0.48	75.64
	+0.51	+1.52	+1.08	+1.66	+2.57	+3.88	-1.73	+3.58	+2.72	+3.45	+3.91	+2.89	+2.17
CorAtt-MIX	70.12 ± 2.26	75.46 ± 2.16	68.20 ± 1.16	66.42 ± 0.87	66.33 ± 0.80	68.45 ± 1.05	69.61 ± 0.98	75.60 ± 0.32	79.14 ± 3.09	81.56 ± 0.34	80.30 ± 0.17	79.74 ± 0.43	73.41
+ IW [29]	70.26 ± 2.52	75.64 ± 2.18	68.35 ± 1.07	66.62 ± 0.77	66.55 ± 0.73	68.74 ± 1.28	69.80 ± 0.94	75.99 ± 0.37	81.87 ± 2.75	84.10 ± 0.38	82.88 ± 0.20	82.33 ± 0.45	74.43
+ DAC-SC [56]	69.44 ± 2.35	74.77 ± 2.43	67.55 ± 1.23	65.85 ± 0.83	65.80 ± 0.85	67.76 ± 1.21	68.93 ± 0.99	74.92 ± 0.35	80.88 ± 2.93	83.39 ± 0.35	82.12 ± 0.19	81.41 ± 0.47	73.57
+ RIW [56]	70.28 ± 2.37	75.71 ± 2.50	68.43 ± 1.29	66.65 ± 0.85	66.56 ± 0.95	68.82 ± 1.12	69.86 ± 1.04	75.98 ± 0.35	81.93 ± 2.61	84.13 ± 0.39	82.93 ± 0.18	82.40 ± 0.49	74.47
+ DRIW [9]	70.54 ± 2.43	75.96 ± 2.36	68.64 ± 1.24	66.84 ± 0.79	66.77 ± 0.73	69.00 ± 1.11	70.06 ± 1.13	76.25 ± 0.36	82.03 ± 2.67	84.33 ± 0.40	83.08 ± 0.22	82.56 ± 0.53	74.67
+ CorSW-OLM (Ours)	70.88 ± 2.26	75.58 ± 2.16	68.51 ± 1.30	67.95 ± 0.59	69.71 ± 0.67	71.73 ± 0.31	68.26 ± 0.52	79.90 ± 1.11	81.66 ± 1.39	85.60 ± 0.88	83.38 ± 1.47	82.24 ± 0.69	75.45
	+0.76	+0.12	+0.31	+1.53	+3.38	+3.28	-1.35	+4.30	+2.52	+4.04	+3.08	+2.50	+2.04

Table 4: Cross-session comparison with manifold-based EEG adaptation baselines.

Method	MI	SSVEP	ERN
SPDDSMBN [53]	69.38 ± 2.11	64.72 ± 0.95	74.86 ± 0.88
Deep OT-SPD [49]	69.91 ± 2.35	63.85 ± 1.02	75.43 ± 1.12
SPDIM [57]	70.52 ± 2.08	65.31 ± 0.89	76.12 ± 0.94
CorAtt-OLM	72.62 ± 2.26	67.15 ± 0.82	80.78 ± 0.66
CorAtt+CorSW	73.40 ± 2.30	69.78 ± 1.15	83.30 ± 1.05

CorAtt-LSM. The number of slicing directions is set to $S = 400$, and the Wasserstein order is fixed to $p = 2$ unless otherwise specified.

Baselines. We consider a diverse set of baselines. Specifically, we include widely used Euclidean deep learning models for EEG decoding, including ShallowConvNet [73], EEGNet [55], MBEEGSE [4], and FBCNet [58]. To highlight the benefit of correlation geometry, we further compare with representative Riemannian and geometric deep learning approaches, namely MAtt [64] and GDLNet [78]. For DG, we additionally compare with several classical instance-level alignment methods, including IW [29], DAC-SC [56], RIW [8], and DRIW [9]. We also report targeted comparisons with manifold-based domain adaptation methods, including SPDDSMBN [53], Deep OT-SPD [49], and SPDIM [57].

Implementation Details. For the BCIC-IV-2a dataset, the number of subparts, the size of the transformation matrix in CorAtt, the learning rate, and the batch size are set to 3, 25×25 , 5×10^{-4} , and 128, respectively. For the MAMEM-SSVEP-II dataset, these values are configured as 7, 15×15 , 5×10^{-3} , and 64. For the BCI-ERN dataset, we use 3 subparts, a transformation matrix of size 14×14 , a learning rate of 1×10^{-3} , and a batch size of 32. All models are trained using the Adam optimizer [52] with identical training schedules.

4.4 Performance Comparison

Evaluation Protocols. We evaluate both predictive performance and robustness to domain shifts under two cross-session protocols.

(1) *Standard cross-session evaluation.* Following prior works [43, 64], we adopt task-specific cross-session splits. For each dataset, one session is designated as the test domain, while the remaining session(s) are used for training and validation. Specifically, for the MI task, the first session is used for training, with one-eighth (12.5%) of trials randomly reserved for validation, and the second session is used for testing. For the SSVEP and ERN tasks, the first three sessions are used for training, the fourth session is fixed for validation, and the fifth session is used for testing. This protocol is employed in Tab. 2 to enable direct and fair comparison with Euclidean and Riemannian baselines reported in prior studies.

(2) *Exhaustive cross-session domain generalization evaluation.* We further adopt an exhaustive transfer protocol that enumerates multiple train→test session splits to assess robustness under diverse session-wise domain shifts. We denote by $ST \rightarrow SE$ a cross-session transfer setting, where the model is trained on sessions indexed by T and evaluated on the held-out session(s) indexed by E . For the MI task, we report bidirectional transfers $S1 \rightarrow S2$ and $S2 \rightarrow S1$. For the SSVEP and ERN tasks, which consist of five sessions, we adopt a leave-one-session-out protocol, yielding five transfers: $S1234 \rightarrow S5$, $S2345 \rightarrow S1$, $S1345 \rightarrow S2$, $S1245 \rightarrow S3$, and $S1235 \rightarrow S4$.

Comparison with Existing EEG Baselines. As shown in Tab. 2, geometry-aware methods consistently outperform Euclidean baselines across the three EEG paradigms. Euclidean models such as EEGNet [55] and ShallowConvNet [73] operate in standard feature spaces and show clear performance gaps, especially on MI and SSVEP. Riemannian models, including MAtt [64] and GDLNet [78], improve over these Euclidean baselines by exploiting second-order EEG geometry. Among them, CorAtt [43] provides a strong correlation-manifold backbone.

Building on CorAtt, CorSW further improves performance across different geometric instantiations. CorAtt-OLM+CorSW-OLM achieves the largest gain on ERN, CorAtt-LSM+CorSW-LSM performs best on SSVEP, and CorAtt-MIX+CorSW-OLM obtains the highest MI accuracy. In addition to improving the mean score, CorSW often reduces run-to-run variability. For example, the standard deviation

Table 5: Effect of reference construction.

Reference	SSVEP	ERN
Gaussian (random)	68.58 ± 1.01	81.33 ± 1.14
Gaussian (fixed)	68.07 ± 1.45	80.76 ± 1.29
Gaussian (matched)	68.24 ± 1.08	81.03 ± 1.17
Source-mix	67.73 ± 1.18	80.47 ± 1.21

Table 6: Effect of correlation embedding.

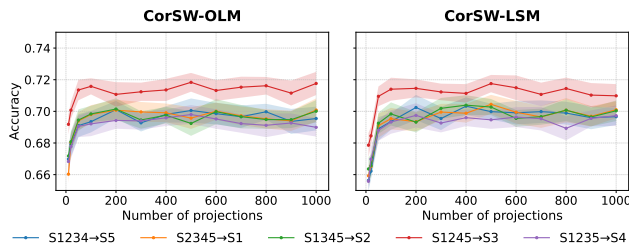
Embedding	SSVEP	ERN
Lower-tri. vec.	65.58 ± 0.68	74.63 ± 1.72
Full-matrix vec.	66.49 ± 0.71	75.15 ± 1.21
Log ^o	68.58 ± 1.01	81.33 ± 1.14
Log [*]	67.74 ± 2.44	78.63 ± 3.31

Table 7: Effect of slicing directions.

Direction	SSVEP	ERN
Random	67.76 ± 1.07	80.47 ± 1.18
Learnable	68.31 ± 1.04	81.02 ± 1.16
Uniform (Ours)	68.58 ± 1.01	81.33 ± 1.14

Table 8: Training time per iteration (ms/iter).

Method	CorAtt	+IW	+DAC-SC	+DRIW	+CorSW
Time	27.50±0.66	29.57±0.63	32.10±0.88	32.23±0.68	32.73±0.97

**Figure 2: Performance of CorSW-OLM/LSM vs. slicing number S on the MAMEM-SSVEP-II dataset.**

of CorAtt-OLM decreases from 3.22 to 1.01 on SSVEP and from 3.40 to 1.14 on ERN after adding CorSW. These results indicate that CorSW provides complementary distribution-level regularization beyond the backbone architecture, improving training stability under session-wise shifts without changing the inference pipeline.

Comparison with DG Strategies. Tab. 3 evaluates robustness under the exhaustive cross-session DG protocol. To ensure a controlled comparison, we fix CorAtt as the backbone and add different DG objectives, including instance-level alignment and whitening-based strategies. The *Mean* column averages performance over all 12 train→test transfers. Across OLM, LSM, and MIX backbones, CorSW achieves the highest mean score among the compared DG methods, improving CorAtt-OLM, CorAtt-LSM, and CorAtt-MIX by +2.45, +2.17, and +2.04, respectively. The gains are especially pronounced on SSVEP and ERN, where the leave-one-session-out protocol exposes more diverse session-wise shifts. Although CorSW is not uniformly better on every split, such as the SSVEP S1235 → S4 transfer, its improvements on the remaining transfers dominate the overall average. On MI, the gains are smaller, which is expected because only two sessions are available and the evaluation contains fewer transfer directions. Overall, these results show that aligning source-domain distributions on the correlation manifold is more effective than applying Euclidean alignment losses to correlation manifold-valued EEG representations.

Ablation Study of CorSW Components. We ablate three key design choices of CorSW: the reference distribution, the correlation embedding, and the slicing directions.

First, Tab. 5 studies how the reference distribution Q^d is constructed. We compare four choices: a Gaussian reference resampled

at each iteration, a fixed Gaussian sampled once before training, a moment-matched Gaussian estimated from training features, and a source-mix reference built from source-domain statistics. The resampled Gaussian performs best on both SSVEP and ERN. Its moderate but consistent gains over the fixed and moment-matched Gaussians suggest that resampling acts as mild stochastic regularization and prevents the model from overfitting to a single finite alignment target. The source-mix reference performs worst, indicating that directly reusing source statistics can introduce source-specific bias rather than providing a neutral common target.

Second, Tab. 6 evaluates whether the pullback embedding ϕ is necessary. We replace the geometry-aware mappings with two flat SW baselines that vectorize either the lower-triangular part or the full correlation matrix before applying Euclidean SW. Both flat vectorization baselines substantially underperform the geometry-aware log embeddings, especially on ERN. This confirms that the gain does not come from simply applying SW to matrix entries; the embedding must preserve the correlation manifold geometry in which slicing and Wasserstein matching are performed.

Third, Tab. 7 compares slicing direction strategies. Uniform unit directions achieve the best performance on both tasks. Learnable directions are close to uniform ones but introduce additional optimization complexity without further gains, while non-uniform random directions are less stable and lead to lower performance. We therefore use uniformly sampled directions as the default choice, consistent with the standard SW formulation in the embedding space. Together with the sensitivity analysis in Fig. 2, where performance stabilizes after a moderate number of projections, these results support the default CorSW configuration used in our experiments: a randomly resampled Gaussian reference, the OLM embedding Log^o, and uniform slicing directions.

Effect of the number of projections S . We analyze the sensitivity of CorSW to the number of slicing projections S in Fig. 2. When S is small, both CorSW-OLM and CorSW-LSM degrade noticeably, indicating that too few directions provide a poor approximation of the SW discrepancy on the correlation manifold. As S increases, performance improves rapidly and then becomes stable, reflecting a more accurate Monte Carlo estimate of the SW distance. Beyond a moderate threshold, additional projections bring only marginal gains, suggesting that the SW approximation has effectively converged. This trend justifies using $S = 400$ as the default setting, which lies in the stable regime while keeping the computation manageable. Thus, CorSW is robust to the choice of S in the large-projection regime and provides a practical accuracy–efficiency trade-off.

Training Efficiency. Tab. 8 reports the per-iteration training time under the same implementation setting. CorSW increases the training time from 27.50 ms/iter to 32.73 ms/iter, adding about 5.2 ms per iteration. This overhead is comparable to DAC-SC and

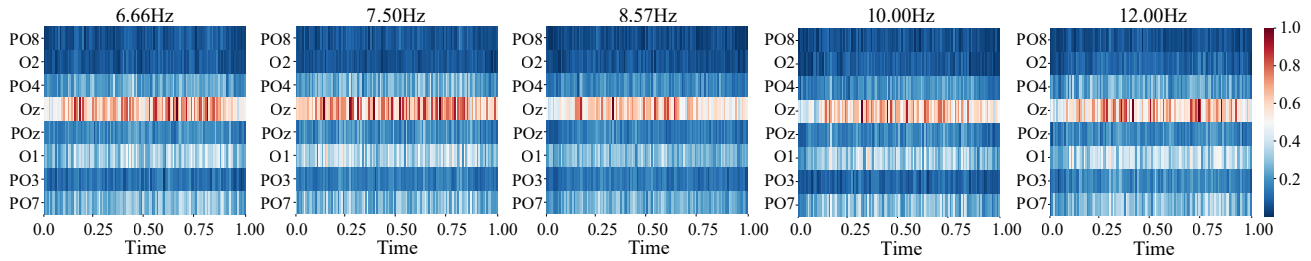


Figure 3: Heatmaps of CorAtt-OLM+CorSW-OLM for the S11 subject across five different frequencies on the MAMEM-SSVEP-II dataset. The x-axis and y-axis represent time and EEG channels, respectively.



Figure 4: The diagram of electrode distribution (a) and the spatial topo-maps of CorAtt-OLM+CorSW-OLM for the S11 subject across five different frequencies on the MAMEM-SSVEP-II dataset. Strong gradient activations are marked in dark red.

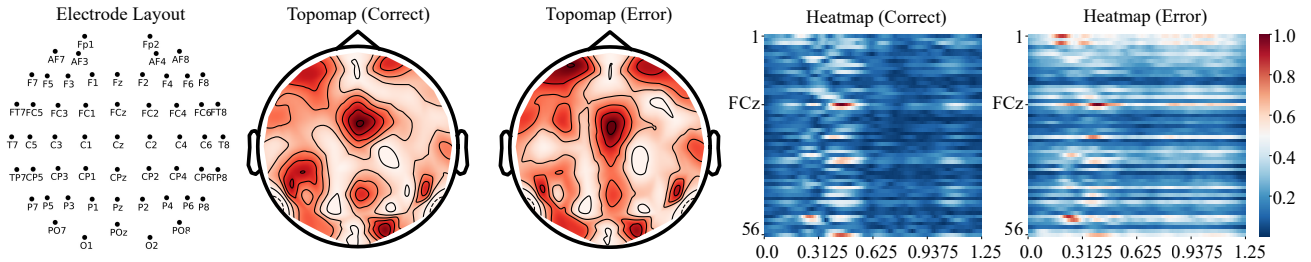


Figure 5: Visualization of heatmaps, topo-maps, and electrode distribution for subject S7 on the BCI-ERN dataset.

DRIW. The additional cost mainly comes from embedding feature-level correlation matrices and computing standard Euclidean SW projections in the embedding space. Since CorSW is used only as a training loss, it does not modify the backbone architecture or introduce any inference-time overhead.

4.5 EEG Model Interpretation

We further examine whether the learned correlation representations focus on neurophysiologically meaningful spatial-temporal patterns by visualizing gradient-based attribution maps of the trained CorAtt-OLM+CorSW-OLM model. For the MAMEM task, as shown in Figs. 3 and 4, CorAtt-OLM+CorSW exhibits pronounced responses around the Oz electrode across all stimulus frequencies, particularly within the 0.25 to 0.75-second window corresponding to canonical SSVEP activity. This spatial-temporal pattern is highly consistent with established neuroscience findings that SSVEP responses are dominated by the primary visual cortex [40, 41], indicating that the learned correlation representations capture meaningful visual processing dynamics rather than session-specific artifacts.

As shown in Fig. 5, for the BCI-ERN dataset, gradient responses distinguishing *correct* and *error* trials are primarily concentrated

around the FCz electrode, with peak activations occurring between 0.1 and 0.4 seconds. This observation aligns well with prior neurophysiological evidence that ERN originates from the anterior cingulate cortex and medial frontal regions involved in performance monitoring [39], suggesting that the model focuses on task-relevant neural signatures rather than session-specific artifacts.

5 Conclusion

We introduced a PEMSW framework for probability measures on manifolds endowed with pullback Euclidean metrics. PEMSW extends sliced-Wasserstein distances to non-Euclidean domains by reducing geodesic slicing on manifolds to linear slicing in an embedding space, yielding a principled and efficient geometry-aware discrepancy. We instantiated this framework on the correlation manifold under OLM and LSM geometries, resulting in CorSW with closed-form slicing coordinates. Moreover, we showed that the SPDSW is exactly recovered as a special case of PEMSW, providing a unified geometric perspective. Overall, PEMSW offers a general and extensible approach for distribution comparison on pullback manifolds, with CorSW serving as an effective realization for correlation-based representations.

Limitations and Ethical Considerations

A main limitation of this work is that the proposed PEMS framework is restricted to manifolds endowed with pullback Euclidean metrics. Although this setting covers important matrix manifolds, including SPD and full-rank correlation manifolds, its direct extension to general Riemannian manifolds without global diffeomorphic embeddings remains unexplored.

From an ethical perspective, this study uses existing EEG benchmarks and does not collect new human-subject data or introduce new clinical interventions. Nevertheless, EEG signals are sensitive biomedical data and may contain information related to cognitive states, health conditions, or individual identity. Any practical use of CorSW-based models should therefore follow strict data governance, including informed consent, secure storage, controlled access, and privacy protection. For applications such as brain-computer interfaces or clinical decision support, model predictions should not be treated as standalone medical decisions.

GenAI Disclosure

Generative AI tools were used to assist with language polishing and LaTeX formatting during manuscript preparation. All technical content, mathematical formulations, experimental design, and results were conceived, implemented, and verified by the authors.

Acknowledgments

This work was supported in part by the Zhejiang Leading Innovative and Entrepreneur Team Introduction Program (2024R01007), and the “Pioneer” and “Leading Goose” Research and Development Program of Zhejiang (2025C02077), the National Natural Science Foundation of China (Grant Nos. 62306127 and 62332008), the National Key R&D Program of China (Grant Nos. 2023YFF1105102 and 2023YFF1105105), the Natural Science Foundation of Jiangsu Province (BK20231040), the Fundamental Research Funds for the Central Universities (JUSRP124015), the Postgraduate Research & Practice Innovation Program of Jiangsu Province (SJCX25_1319).

References

- [1] Khald Ali I. Aboalayon, Miad Faezipour, Wafaa S. Almuhammadi, and Saeid Moslehpour. 2016. Sleep Stage Classification Using EEG Signal Analysis: A Comprehensive Survey and New Investigation. *Entropy* 18, 9 (2016), 272.
- [2] Ijaz Ahmad, Xin Wang, Mingxing Zhu, Cheng Wang, Yao Pi, Javed Ali Khan, Siyab Khan, Oluwarotimi Williams Samuel, Shixiong Chen, and Guanglin Li. 2022. EEG-Based Epileptic Seizure Detection via Machine/Deep Learning Approaches: A Systematic Review. *Computational Intelligence and Neuroscience* 2022 (2022), 6486570.
- [3] H. Altaheri, G. Muhammad, M. Alsulaiman, S. U. Amin, G. A. Altuwajiri, W. Abdul, M. A. Bencherif, and M. Faisal. 2023. Deep learning techniques for classification of electroencephalogram (EEG) motor imagery (MI) signals: A review. *Neural Computing and Applications* 35, 20 (2023), 14681–14722.
- [4] Ghadir Ali Altuwajiri, Ghulam Muhammad, Hamdi Altaheri, and Mansour Alsulaiman. 2022. A multi-branch convolutional neural network with squeeze-and-excitation attention blocks for EEG-based motor imagery signals classification. *Diagnostics* 12, 4 (2022), 995.
- [5] Ilya Archakov and Peter Reinhard Hansen. 2021. A New Parametrization of Correlation Matrices. *Econometrica* 89, 4 (2021), 1699–1715. doi:10.3982/ECTA16910
- [6] Erhan Bayraktar and Gaoyue Guo. 2021. Strong equivalence between metrics of Wasserstein type. *Electronic Communications in Probability* 26 (2021), 1–13.
- [7] Rajendra Bhatia. 2009. *Positive Definite Matrices*. Princeton University Press, Princeton, NJ, USA.
- [8] Qi Bi, Jingjun Yi, Hao Zheng, Wei Ji, Yawen Huang, Yuexiang Li, and Yefeng Zheng. 2024. Learning Generalized Medical Image Segmentation from Decoupled Feature Queries. In *Proceedings of the AAAI Conference on Artificial Intelligence*, Vol. 38. 810–818.
- [9] Qi Bi, Jingjun Yi, Hao Zheng, Wei Ji, Yawen Huang, Yuexiang Li, and Yefeng Zheng. 2025. Learning Generalized Medical Image Representation by Decoupled Feature Queries. *IEEE Transactions on Pattern Analysis and Machine Intelligence* 47, 12 (2025), 11252–11269.
- [10] Wouter Biesmans, Neetha Das, Tom Francart, and Alexander Bertrand. 2016. Auditory-inspired speech envelope extraction methods for improved EEG-based auditory attention detection in a cocktail party scenario. *IEEE Transactions on Neural Systems and Rehabilitation Engineering* 25, 5 (2016), 402–412.
- [11] Benjamin Blankertz, Ryota Tomioka, Steven Lemm, Motoaki Kawanabe, and Klaus-Robert Muller. 2007. Optimizing spatial filters for robust EEG single-trial analysis. *IEEE Signal processing magazine* 25, 1 (2007), 41–56.
- [12] Clément Bonet, Paul Berg, Nicolas Courty, François Septier, Lucas Drumetz, and Minh-Tan Pham. 2023. Spherical Sliced-Wasserstein. In *International Conference on Learning Representations*. OpenReview.net, Kigali, Rwanda, 9 pages.
- [13] Clément Bonet, Laetitia Chapel, Lucas Drumetz, and Nicolas Courty. 2023. Hyperbolic Sliced-Wasserstein via Geodesic and Horospherical Projections. In *Proceedings of the 2nd Annual Workshop on Topology, Algebra, and Geometry in Machine Learning at the 40th International Conference on Machine Learning*. PMLR, Honolulu, Hawaii, USA, 12 pages.
- [14] Clément Bonet, Benoit Malézieux, Alain Rakotomamonjy, Lucas Drumetz, Thomas Moreau, Matthieu Kowalski, and Nicolas Courty. 2023. Sliced-Wasserstein on symmetric positive definite matrices for M/EEG signals. In *International Conference on Machine Learning*. PMLR, Honolulu, Hawaii, USA, 2777–2805.
- [15] Nicolas Bonneel, Julien Rabin, Gabriel Peyré, and Hanspeter Pfister. 2015. Sliced and Radon Wasserstein Barycenters of Measures. *Journal of Mathematical Imaging and Vision* 51, 1 (2015), 22–45. doi:10.1007/s10851-014-0506-3
- [16] Nicolas Bonnotte. 2013. *Unidimensional and evolution methods for optimal transportation*. Ph.D. Dissertation. Paris 11.
- [17] Martin R Bridson and André Haefliger. 2013. *Metric spaces of non-positive curvature*. Vol. 319. Springer Science & Business Media.
- [18] Daniel Brooks, Olivier Schwander, Frédéric Barbaresco, Jean-Yves Schneider, and Matthieu Cord. 2019. Riemannian batch normalization for SPD neural networks. In *Advances in Neural Information Processing Systems*, Vol. 32. Curran Associates, Inc., Vancouver, Canada, 8890–8901.
- [19] Clemens Brunner, Robert Leeb, Gernot Müller-Putz, Alois Schlögl, and Gert Pfurtscheller. 2008. BCI Competition 2008–Graz Data Set A. *Institute for Knowledge Discovery (Laboratory of Brain-Computer Interfaces), Graz University of Technology* (2008).
- [20] Rudrasis Chakraborty, Jose Bouza, Jonathan Manton, and Baba C Vemuri. 2022. ManifoldNet: A Deep Neural Network for Manifold-Valued Data With Applications. *IEEE Transactions on Pattern Analysis and Machine Intelligence* 44, 2 (2022), 799–810.
- [21] Ziheng Chen, Yue Song, Gaowen Liu, Ramana Rao Kompella, Xiao-Jun Wu, and Nicu Sebe. 2024. Riemannian Multinomial Logistics Regression for SPD Neural Networks. In *Proceedings of the IEEE/CVF Conference on Computer Vision and Pattern Recognition*. 17086–17096.
- [22] Ziheng Chen, Yue Song, Yunmei Liu, and Nicu Sebe. 2024. A Lie Group Approach to Riemannian Batch Normalization. In *International Conference on Learning Representations*. OpenReview.net, Vienna, Austria.
- [23] Ziheng Chen, Yue Song, Rui Wang, Xiaojun Wu, and Nicu Sebe. 2024. RMLR: Extending Multinomial Logistic Regression into General Geometries. In *Advances in Neural Information Processing Systems*.
- [24] Ziheng Chen, Yue Song, Xiao-Jun Wu, Gaowen Liu, and Nicu Sebe. 2025. Understanding Matrix Function Normalizations in Covariance Pooling Through the Lens of Riemannian Geometry. In *International Conference on Learning Representations*.
- [25] Ziheng Chen, Yue Song, Xiao-Jun Wu, and Nicu Sebe. 2025. Gyrogroup Batch Normalization. In *International Conference on Learning Representations*.
- [26] Ziheng Chen, Yue Song, Tianyang Xu, Zhiwu Huang, Xiao-Jun Wu, and Nicu Sebe. 2024. Adaptive Log-Euclidean Metrics for SPD Matrix Learning. *IEEE Transactions on Image Processing* 33 (2024), 5194–5205.
- [27] Ziheng Chen, Tianyang Xu, Xiao-Jun Wu, Rui Wang, Zhiwu Huang, and Josef Kittler. 2023. Riemannian Local Mechanism for SPD Neural Networks. In *Proceedings of the AAAI Conference on Artificial Intelligence*.
- [28] Resmi Cherian and E. Gracemary Kanaga. 2022. Theoretical and Methodological Analysis of EEG Based Seizure Detection and Prediction: An Exhaustive Review. *Journal of Neuroscience Methods* 369 (2022), 109483.
- [29] Sungha Choi, Sanghun Jung, Huiwon Yun, Joanne T. Kim, Seungryong Kim, and Jaegul Choo. 2021. RobustNet: Improving Domain Generalization in Urban-Scene Segmentation via Instance Selective Whitening. In *Proceedings of the IEEE/CVF Conference on Computer Vision and Pattern Recognition*. 11580–11590.
- [30] Marco Congedo, Alexandre Barachant, and Rajendra Bhatia. 2017. Riemannian geometry for EEG-based brain-computer interfaces; a primer and a review. *Brain-Computer Interfaces* 4, 3 (2017), 155–174.
- [31] Li Cui, Xin Qi, Chengfeng Wen, Na Lei, Xinyuan Li, Min Zhang, and Xianfeng Gu. 2019. Spherical optimal transportation. *Computer-Aided Design* 115 (2019), 181–193.

- [32] Marco Cuturi. 2013. Sinkhorn distances: Lightspeed computation of optimal transport. In *Advances in Neural Information Processing Systems*, Vol. 26. Curran Associates, Inc., Lake Tahoe, Nevada, USA, 2292–2300.
- [33] D. Dadebayev, W. W. Goh, and E. X. Tan. 2022. EEG-based emotion recognition: Review of commercial EEG devices and machine learning techniques. *Journal of King Saud University-Computer and Information Sciences* 34, 7 (2022), 4385–4401.
- [34] Paul David and Weiqing Gu. 2019. A Riemannian Structure for Correlation Matrices. *Operators and Matrices* 13, 3 (2019), 607–627.
- [35] Manfredo Perdigão Do Carmo and Francis J. Flaherty. 1992. *Riemannian Geometry*. Springer, New York, NY, USA.
- [36] Sacha Epskamp and Eiko I Fried. 2018. A Tutorial on Regularized Partial Correlation Networks. *Psychological Methods* 23, 4 (2018), 617–634.
- [37] Kilian Fatras, Younes Zine, Rémi Flamary, Rémi Gribonval, and Nicolas Courty. 2020. Learning with minibatch Wasserstein: asymptotic and gradient properties. In *Proceedings of the Twenty Third International Conference on Artificial Intelligence and Statistics*, Vol. 108. PMLR, Online, 2131–2141.
- [38] Nicolas Fournier and Arnaud Guillin. 2015. On the rate of convergence in Wasserstein distance of the empirical measure. *Probability Theory and Related Fields* 162, 3 (2015), 707–738.
- [39] Greg Hajcak. 2012. What We’ve Learned From Mistakes: Insights From Error-Related Brain Activity. *Current Directions in Psychological Science* 21, 2 (2012), 101–106.
- [40] Chengcheng Han, Guanghua Xu, Jun Xie, Chaoyang Chen, and Sicong Zhang. 2018. Highly Interactive Brain-Computer Interface Based on Flicker-Free Steady-State Motion Visual Evoked Potential. *Scientific Reports* 8, 1 (2018), 5835.
- [41] Christoph S Herrmann. 2001. Human EEG Responses to 1–100 Hz Flicker: Resonance Phenomena in Visual Cortex and Their Potential Correlation to Cognitive Phenomena. *Experimental Brain Research* 137, 3–4 (2001), 346–352.
- [42] Gabriel Emile Hine, Emanuele Maiorana, and Patrizio Campisi. 2017. Resting-state EEG: A study on its non-stationarity for biometric applications. In *Proceedings of the 2017 International Conference of the Biometrics Special Interest Group (BIOSIG)*. IEEE, 1–5.
- [43] Chen Hu, Rui Wang, Xiaoning Song, Tao Zhou, Xiao-Jun Wu, Nicu Sebe, and Ziheng Chen. 2025. A correlation manifold self-attention network for EEG decoding. In *Proceedings of the Thirty-Fourth International Joint Conference on Artificial Intelligence*. 5372–5380.
- [44] Zhiwu Huang and Luc Van Gool. 2017. A Riemannian network for SPD matrix learning. In *Proceedings of the Thirty-First AAAI Conference on Artificial Intelligence*, Vol. 31. 2036–2042.
- [45] Zhiwu Huang, Jiqing Wu, and Luc Van Gool. 2018. Building deep networks on Grassmann manifolds. In *Proceedings of the AAAI Conference on Artificial Intelligence*, Vol. 32. AAAI Press, New Orleans, LA, USA, 3279–3286.
- [46] Thorir Mar Ingólfsson, Michael Hersche, Xiaying Wang, Nobuaki Kobayashi, Lukas Cavigelli, and Luca Benini. 2020. EEG-TCNet: An accurate temporal convolutional network for embedded motor-imagery brain-machine interfaces. In *IEEE International Conference on Systems, Man, and Cybernetics*. 2958–2965.
- [47] Mahdi Jalili and Maria G Knyazeva. 2011. Constructing Brain Functional Networks From EEG: Partial and Unpartial Correlations. *Journal of Integrative Neuroscience* 10, 2 (2011), 213–232.
- [48] Ce Ju and Cuntai Guan. 2023. Graph Neural Networks on SPD Manifolds for Motor Imagery Classification: A Perspective From the Time-Frequency Analysis. *IEEE Transactions on Neural Networks and Learning Systems* 35, 12 (2023), 17701–17715.
- [49] Ce Ju and Cuntai Guan. 2025. Deep optimal transport for domain adaptation on SPD manifolds. *Artificial Intelligence* 345 (2025), 104347.
- [50] Ce Ju, Reinmar J Kobler, Antoine Collas, Motoaki Kawanabe, Cuntai Guan, and Bertrand Thirion. 2025. SPD Learning for Covariance-Based Neuroimaging Analysis: Perspectives, Methods, and Challenges. *arXiv:2504.18882* (2025).
- [51] Ce Ju, Reinmar J Kobler, Liyao Tang, Cuntai Guan, and Motoaki Kawanabe. 2024. Deep Geodesic Canonical Correlation Analysis for Covariance-Based Neuroimaging Data. In *International Conference on Learning Representations*. OpenReview.net, Vienna, Austria, 9 pages.
- [52] Diederik P. Kingma and Jimmy Ba. 2017. Adam: A Method for Stochastic Optimization. *arXiv:Preprint [cs.LG]* <https://arxiv.org/abs/1412.6980>
- [53] Reinmar Kobler, Jun-ichiro Hirayama, Qibin Zhao, and Motoaki Kawanabe. 2022. SPD domain-specific batch normalization to crack interpretable unsupervised domain adaptation in EEG. In *Advances in Neural Information Processing Systems*, Vol. 35. 6219–6235.
- [54] Soheil Kolouri, Yang Zou, and Gustavo K Rohde. 2016. Sliced Wasserstein Kernels for Probability Distributions. In *Proceedings of the IEEE Conference on Computer Vision and Pattern Recognition*. IEEE, 5258–5267.
- [55] Vernon J Lawhern, Amelia J Solon, Nicholas R Waytowich, Stephen M Gordon, Chou P Hung, and Brent J Lance. 2018. EEGNet: a compact convolutional neural network for EEG-based brain–computer interfaces. *Journal of Neural Engineering* 15, 5 (2018), 056013.
- [56] Sangrok Lee, Jongseong Bae, and Ha Young Kim. 2023. Decompose, adjust, compose: Effective normalization by playing with frequency for domain generalization. In *Proceedings of the IEEE/CVF conference on computer vision and pattern recognition*. 11776–11785.
- [57] Shanglin Li, Motoaki Kawanabe, and Reinmar Kobler. 2025. SPDIM: Source-Free Unsupervised Conditional and Label Shift Adaptation in EEG. In *International Conference on Representation Learning*, Vol. 2025.
- [58] Ravikiran Mane, Effie Chew, Karen Chua, Kai Keng Ang, Neethu Robinson, A Prasad Vinod, Seong-Whan Lee, and Cuntai Guan. 2021. FBCNet: A multi-view convolutional neural network for brain-computer interface. *arXiv preprint arXiv:2104.01233* (2021), 16 pages.
- [59] Perrin Margaux, Emmanuel Maby, Sébastien Daligault, Olivier Bertrand, and Jérémie Mattout. 2012. Objective and Subjective Evaluation of Online Error Correction During P300-Based Spelling. *Advances in Human-Computer Interaction* 2012 (2012), 1–13.
- [60] Robert J McCann. 2001. Polar factorization of maps on Riemannian manifolds. *Geometric & Functional Analysis GAFA* 11, 3 (2001), 589–608.
- [61] Kimia Nadjahi, Alain Durmus, Lénaïc Chizat, Soheil Kolouri, Shahin Shahrampour, and Umüt Simsekli. 2020. Statistical and Topological Properties of Sliced Probability Divergences. In *Advances in Neural Information Processing Systems* 33. 20802–20812.
- [62] Kimia Nadjahi, Alain Durmus, Umüt Şimşekli, and Roland Badeau. 2019. Asymptotic Guarantees for Learning Generative Models With the Sliced-Wasserstein Distance. In *Advances in Neural Information Processing Systems*. 1–12.
- [63] Spiros Nikolopoulos. 2016. MAMEM EEG SSVEP Dataset II (256 Channels, 11 Subjects, 5 Frequencies Presented Simultaneously). Dataset. <https://api.semanticscholar.org/CorpusID:63262529>
- [64] Yue-Ting Pan, Jing-Lun Chou, and Chun-Shu Wei. 2022. MAtt: A Manifold Attention Network for EEG Decoding. In *Advances in Neural Information Processing Systems*, Vol. 35. 31116–31129.
- [65] François-Pierre Paty and Marco Cuturi. 2019. Subspace Robust Wasserstein Distances. In *Proceedings of the 36th International Conference on Machine Learning*, Vol. 97. PMLR, 5072–5081. doi:10.5555/3327144.3327253
- [66] Ofir Pele and Michael Werman. 2009. Fast and Robust Earth Mover’s Distances. In *IEEE 12th International Conference on Computer Vision*. IEEE, 460–467.
- [67] Gabriel Peyré and Marco Cuturi. 2019. Computational Optimal Transport: With Applications to Data Science. *Foundations and Trends in Machine Learning* 11, 5-6 (2019), 355–607.
- [68] H. Phan and K. Mikkelsen. 2022. Automatic sleep staging of EEG signals: Recent development, challenges, and future directions. *Physiological Measurement* 43, 4 (2022), 04TR01.
- [69] Julien Rabin, Gabriel Peyré, Julie Delon, and Marc Bernot. 2011. Wasserstein Barycenter and Its Application to Texture Mixing. In *International Conference on Scale Space and Variational Methods in Computer Vision*. Springer, Berlin, Heidelberg, Germany, 435–446. doi:10.1007/978-3-642-24785-9_37
- [70] Alain Rakotomamonjy, Mokhtar Z Alaya, Maxime Berar, and Gilles Gasso. 2021. Statistical and Topological Properties of Gaussian Smoothed Sliced Probability Divergences. *arXiv preprint arXiv:2110.10524* (2021).
- [71] Riccardo Rebonato and Peter Jäckel. 2011. *The most general methodology to create a valid correlation matrix for risk management and option pricing purposes*. Technical Report. Available at SSRN 1969689.
- [72] Subhrajit Roy, Isabell Kiral-Kornek, and Stefan Harrer. 2019. ChronoNet: A deep recurrent neural network for abnormal EEG identification. In *Conference on Artificial Intelligence in Medicine*, Vol. 11526. 47–56.
- [73] Robin Tibor Schirrmester, Jost Tobias Springenberg, Lukas Dominique Josef Fiederer, Martin Glasstetter, Katharina Eggenesperger, Michael Tangermann, Frank Hutter, Wolfram Burgard, and Tonio Ball. 2017. Deep learning with convolutional neural networks for EEG decoding and visualization. *Human Brain Mapping* 38, 11 (2017), 5391–5420.
- [74] Nazmi Sofian Suhaimi, James Mountstephens, Jason Teo, et al. 2020. EEG-based emotion recognition: A state-of-the-art review of current trends and opportunities. *Computational Intelligence and Neuroscience* 2020 (2020), 9814248.
- [75] Yann Thanwerdas. 2024. Permutation-Invariant Log-Euclidean Geometries on Full-Rank Correlation Matrices. *SIAM J. Matrix Anal. Appl.* 45, 2 (2024), 930–952.
- [76] Loring W. Tu. 2011. *An Introduction to Manifolds*. Springer, New York, NY, USA.
- [77] Cédric Villani. 2009. *Optimal Transport: Old and New*. Grundlehren der Mathematischen Wissenschaften, Vol. 338. Springer, Berlin, Heidelberg, Germany.
- [78] Rui Wang, Chen Hu, Ziheng Chen, Xiao-Jun Wu, and Xiaoning Song. 2024. A Grassmannian Manifold Self-Attention Network for Signal Classification. In *Proceedings of the International Joint Conference on Artificial Intelligence*. 5099–5107.
- [79] Rui Wang, Shaocheng Jin, Ziheng Chen, Xiaoqing Luo, and Xiao-Jun Wu. 2025. Learning to Normalize on the SPD Manifold under Bures-Wasserstein Geometry. In *Proceedings of the IEEE/CVF Conference on Computer Vision and Pattern Recognition*. 8289–8298.
- [80] Or Yair, Felix Dietrich, Ronen Talmon, and Ioannis G Kevrekidis. 2019. Domain Adaptation with Optimal Transport on the Manifold of SPD Matrices. *arXiv preprint arXiv:1906.00616* (2019), 12 pages.

A Related Work

Covariance/Correlation Matrix-Based EEG Decoding. Methods that operate on covariance or correlation matrices have demonstrated strong EEG decoding performance by explicitly modeling the underlying geometry of symmetric positive definite (SPD) manifolds, thereby improving robustness to inter-subject variability and session-wise distribution shifts [30, 50]. MAtt [64] constructs attention mechanisms directly on SPD manifolds, enabling the network to capture spatiotemporal dependencies between EEG channels through geometry-preserving operations, and consistently outperforming conventional Euclidean deep learning baselines. SPDDSMBN [53] focuses on unsupervised domain adaptation by learning domain-invariant mappings in the tangent space of the SPD manifold, where an interpretable normalization scheme is introduced to reduce domain-specific covariance shifts. DGCCA [51] further extends correlation-based modeling by introducing geodesic correlation learning in an SPD latent space, explicitly aligning paired covariance representations across modalities while respecting Riemannian geometry. SPDIM [57] addresses the more challenging source-free domain adaptation setting by enforcing SPD-constrained parameterizations to handle both conditional shift and label shift without access to source-domain data.

Domain Generalization. Domain generalization aims to learn domain-invariant representations from multiple source domains to generalize well to unseen target domains. Recent studies have explored various strategies to align feature distributions or disentangle domain-specific information. IW [29] addresses the issue where standard whitening transformations may eliminate domain-invariant content along with style. It proposes an Instance Selective Whitening (ISW) loss to disentangle domain-specific style (encoded in feature covariance) from domain-invariant content, selectively suppressing only the style-sensitive covariance terms to enhance robustness. DAC-SC [56] approaches domain generalization from a frequency domain perspective, treating amplitude and phase as style and content, respectively. It introduces a Decompose, Adjust, and Compose (DAC) framework with Style-Controlling (SC) normalization to explicitly adjust the degree of style variation while preserving content information. In the context of medical imaging, RIW [8] identifies feature redundancy and misalignment as key barriers to generalization. It proposes a Relaxed Deep Whitening Transformation (RDWT) to minimize channel-wise correlations in a learnable manner, thereby maximizing the expressive power of per-channel representations. Extending this, DRIW [9] introduces a Deep Restricted Isometry Whitening transform. By optimizing the spectral norm to satisfy the restricted isometry property, DRIW theoretically enforces strict orthogonality among feature channels, further reducing redundancy and improving cross-domain feature alignment.

B Proofs of the Theorems in the Main Paper

The proofs are organized following the logical dependencies of the results in the main paper, starting from auxiliary bounds and complexity results, and culminating in the main compactness and convergence theorems.

B.1 Proof of the Thm. 3.1

PROOF OF THM. 3.1. Let $a \in S_{\mathcal{E}}$. We prove Eqs. (11) and (12) by first characterizing the geodesic \mathcal{G}_a in closed form, and then deriving the associated slicing coordinate via geodesic projection.

Part I: Geodesic \mathcal{G}_a in PEMs. Consider the geodesic curve

$$\gamma_a(t) = \phi^{-1}(\phi(x_0) + t a), \quad t \in \mathbb{R}. \quad (37)$$

Then for any $s, t \in \mathbb{R}$, we have

$$\begin{aligned} d_{\mathcal{M}}(\gamma_a(s), \gamma_a(t)) &= d_{\mathcal{M}}(\phi^{-1}(\phi(x_0) + s a), \phi^{-1}(\phi(x_0) + t a)) \\ &\stackrel{(1)}{=} \|(\phi(x_0) + s a) - (\phi(x_0) + t a)\|_{\mathcal{E}} \\ &= \|(s - t)a\|_{\mathcal{E}} \\ &= |s - t| \|a\|_{\mathcal{E}} \\ &\stackrel{(2)}{=} |s - t|. \end{aligned} \quad (38)$$

The derivation of Eq. (38) follows.

(1) follows from the pullback Euclidean distance $d_{\mathcal{M}}(x, y) = \|\phi(x) - \phi(y)\|_{\mathcal{E}}$.

(2) follows from $a \in S_{\mathcal{E}}$, i.e., $\|a\|_{\mathcal{E}} = 1$.

Thus, $\mathcal{G}_a = \{\gamma_a(t) : t \in \mathbb{R}\}$ is a geodesic in \mathcal{M} . We denote this geodesic by

$$\mathcal{G}_a = \{\gamma_a(t) = \phi^{-1}(\phi(x_0) + t a) : t \in \mathbb{R}\}. \quad (39)$$

Part II: Slicing coordinate via geodesic projection. Let $x \in \mathcal{M}$. By definition, the geodesic projection of x onto \mathcal{G}_a is defined as

$$p^{\mathcal{G}_a}(x) = \operatorname{argmin}_{y \in \mathcal{G}_a} d_{\mathcal{M}}(x, y) = \operatorname{argmin}_{t \in \mathbb{R}} d_{\mathcal{M}}(x, \gamma_a(t))^2. \quad (40)$$

Let $f(t) := d_{\mathcal{M}}(x, \gamma_a(t))^2$. Then, we have

$$\begin{aligned} f(t) &= d_{\mathcal{M}}(x, \phi^{-1}(\phi(x_0) + t a))^2 \\ &\stackrel{(1)}{=} \|\phi(x) - \phi(\phi^{-1}(\phi(x_0) + t a))\|_{\mathcal{E}}^2 \\ &\stackrel{(2)}{=} \|\phi(x) - (\phi(x_0) + t a)\|_{\mathcal{E}}^2 \\ &\stackrel{(3)}{=} \langle \phi(x) - \phi(x_0) - t a, \phi(x) - \phi(x_0) - t a \rangle_{\mathcal{E}} \\ &\stackrel{(4)}{=} \langle \phi(x) - \phi(x_0), \phi(x) - \phi(x_0) \rangle_{\mathcal{E}} - t \langle \phi(x) - \phi(x_0), a \rangle_{\mathcal{E}} \\ &\quad - t \langle a, \phi(x) - \phi(x_0) \rangle_{\mathcal{E}} + t^2 \langle a, a \rangle_{\mathcal{E}} \\ &\stackrel{(5)}{=} \|\phi(x) - \phi(x_0)\|_{\mathcal{E}}^2 - 2t \langle a, \phi(x) - \phi(x_0) \rangle_{\mathcal{E}} + t^2 \langle a, a \rangle_{\mathcal{E}} \\ &\stackrel{(6)}{=} \|\phi(x) - \phi(x_0)\|_{\mathcal{E}}^2 - 2t \langle a, \phi(x) - \phi(x_0) \rangle_{\mathcal{E}} + t^2. \end{aligned} \quad (41)$$

The derivation of Eq. (41) follows.

(1) follows from the pullback Euclidean distance $d_{\mathcal{M}}(x, y) = \|\phi(x) - \phi(y)\|_{\mathcal{E}}$.

(2) follows from $\phi \circ \phi^{-1}$ is the identify map.

(3) follows from $\|z\|_{\mathcal{E}}^2 = \langle z, z \rangle_{\mathcal{E}}$.

(4) follows from the bilinearity of $\langle \cdot, \cdot \rangle_{\mathcal{E}}$.

(5) follows from the symmetry of the inner product, $\langle u, v \rangle_{\mathcal{E}} = \langle v, u \rangle_{\mathcal{E}}$, and the definition $\|u\|_{\mathcal{E}}^2 = \langle u, u \rangle_{\mathcal{E}}$.

(6) follows from $a \in S_{\mathcal{E}}$, i.e., $\langle a, a \rangle_{\mathcal{E}} = 1$.

Therefore, $f(t)$ is a quadratic function of t . Its derivative with respect to t is given by

$$f'(t) = -2 \langle a, \phi(x) - \phi(x_0) \rangle_{\mathcal{E}} + 2t. \quad (42)$$

Since $f'(t) = 0$ at the minimizer and $f''(t) = 2 > 0$, the unique minimizer is given by

$$t_a(x) = \langle a, \phi(x) - \phi(x_0) \rangle_{\mathcal{E}}, \quad (43)$$

which yields the slicing coordinate defined in Eq. (12).

Substituting Eq. (43) into the geodesic parametrization Eq. (37), we obtain

$$p^{\mathcal{G}_a}(x) = \gamma_a(t_a(x)) = \phi^{-1}\left(\phi(x_0) + t_a(x) a\right) \in \mathcal{G}_a, \quad (44)$$

which yields the projection formula in Eq. (11). \square

There are two classical approaches to defining coordinates on geodesically complete Riemannian manifolds [13]. The first relies on geodesic projection, as adopted in the previous section, while the second is based on Busemann functions [17]. In the following, we show that on pullback Euclidean manifolds, the Busemann coordinate associated with a geodesic ray admits a closed-form expression and coincides, up to a sign convention, with the slicing coordinate obtained via geodesic projection.

Definition B.1 (Busemann function on PEMs). Let (\mathcal{M}, g) be a geodesically complete pullback Euclidean manifold induced by a diffeomorphism $\phi : \mathcal{M} \rightarrow \mathcal{E}$. Let $a \in S_{\mathcal{E}}$ and let

$$\gamma_a(t) = \phi^{-1}(\phi(x_0) + t a), \quad t \geq 0, \quad (45)$$

be a geodesic ray on \mathcal{M} . The Busemann function associated with γ_a is defined as

$$B_{\gamma_a}(x) = \lim_{t \rightarrow \infty} (d_{\mathcal{M}}(x, \gamma_a(t)) - t), \quad \forall x \in \mathcal{M}. \quad (46)$$

Proposition B.2 (Busemann coordinates on PEMs). Let $a \in S_{\mathcal{E}}$ and let γ_a be the geodesic ray defined above. Then, for any $x \in \mathcal{M}$, the associated Busemann function admits the closed form

$$B_{\gamma_a}(x) = -\langle a, \phi(x) - \phi(x_0) \rangle_{\mathcal{E}}. \quad (47)$$

PROOF OF PROP. B.2. By definition, we have

$$B_{\gamma_a}(x) = \lim_{t \rightarrow \infty} (d_{\mathcal{M}}(x, \gamma_a(t)) - t). \quad (48)$$

Using the pullback Euclidean distance $d_{\mathcal{M}}(x, y) = \|\phi(x) - \phi(y)\|_{\mathcal{E}}$, we obtain

$$\begin{aligned} d_{\mathcal{M}}(x, \gamma_a(t)) - t &= \|\phi(x) - (\phi(x_0) + t a)\|_{\mathcal{E}} - t \\ &= \|\phi(x) - \phi(x_0) - t a\|_{\mathcal{E}} - t. \end{aligned} \quad (49)$$

Let $u = \phi(x) - \phi(x_0) \in \mathcal{E}$. Since $a \in S_{\mathcal{E}}$, it follows from standard Euclidean geometry that

$$\lim_{t \rightarrow \infty} (\|u - t a\|_{\mathcal{E}} - t) = -\langle u, a \rangle_{\mathcal{E}}. \quad (50)$$

Taking the limit in Eq. (49) yields

$$B_{\gamma_a}(x) = -\langle a, \phi(x) - \phi(x_0) \rangle_{\mathcal{E}}, \quad (51)$$

which establishes Eq. (47). \square

Corollary B.3 (Equivalence with slicing coordinates). Let $t_a(x)$ denote the slicing coordinate obtained via geodesic projection. Then

$$B_{\gamma_a}(x) = -t_a(x), \quad (52)$$

and the Busemann projection onto \mathcal{G}_a coincides with the geodesic projection.

PROOF OF COR. B.3. As shown in Prop. B.2, the Busemann coordinate of x is $B_{\gamma_a}(x) = -\langle a, \phi(x) - \phi(x_0) \rangle_{\mathcal{E}}$. On the other hand, the slicing coordinate obtained by geodesic projection satisfies $t_a(x) = \langle a, \phi(x) - \phi(x_0) \rangle_{\mathcal{E}}$. Therefore, $B_{\gamma_a}(x) = -t_a(x)$.

The Busemann projection is defined as the unique point $\gamma_a(t)$ on the geodesic ray sharing the same Busemann coordinate, i.e., $B_{\gamma_a}(x) = B_{\gamma_a}(\gamma_a(t))$. Since $B_{\gamma_a}(\gamma_a(t)) = -t$, we obtain $t = t_a(x)$, which yields

$$p^{\mathcal{G}_a}(x) = \gamma_a(t_a(x)) = \phi^{-1}\left(\phi(x_0) + t_a(x) a\right). \quad (53)$$

Hence, the Busemann projection coincides with the geodesic projection. \square

B.2 Proof of the Lem. 3.3

PROOF OF LEM. 3.3. By the definition of the slicing coordinate in Eq. (12), we have

$$t_a(x) = \langle a, \phi(x) - \phi(x_0) \rangle_{\mathcal{E}}. \quad (54)$$

Let $\pi_a : \mathcal{E} \rightarrow \mathbb{R}$ be defined by $\pi_a(z) = \langle a, z \rangle_{\mathcal{E}}$. Then Eq. (54) can be equivalently written as

$$t_a(x) = \pi_a(\phi(x)) - \pi_a(\phi(x_0)), \quad (55)$$

which establishes Eq. (15).

Let $\tilde{\mu} = \phi_{\#}\mu$. Since $t_a = \tau_{-\pi_a(\phi(x_0))} \circ \pi_a \circ \phi$, where $\tau_c : \mathbb{R} \rightarrow \mathbb{R}$ denotes the translation $\tau_c(s) = s + c$, it follows that

$$t_{a\#\mu} = (\tau_{-\pi_a(\phi(x_0))})_{\#}(\pi_{a\#\tilde{\mu}}). \quad (56)$$

Therefore, $t_{a\#\mu}$ is a translation of $\pi_{a\#\tilde{\mu}}$. It can be readily verified that the same conclusion holds for ν . \square

B.3 Proof of the Thm. 3.4

PROOF OF PEMSW_p(μ, ν) = SW_p($\tilde{\mu}, \tilde{\nu}$). For each $a \in S_{\mathcal{E}}$, we consider the linear functional $z \mapsto \langle a, z \rangle_{\mathcal{E}}$ on \mathcal{E} . By Lem. 3.3, this functional induces the slicing coordinate

$$t_a(x) = \langle a, \phi(x) \rangle_{\mathcal{E}} - \langle a, \phi(x_0) \rangle_{\mathcal{E}}, \quad \forall x \in \mathcal{M}. \quad (57)$$

Let $\tilde{\mu} = \phi_{\#}\mu$ and $\tilde{\nu} = \phi_{\#}\nu$. Using the standard pushforward representation of the p -Wasserstein distance (e.g., [65, Lemma 6]), we obtain

$$\begin{aligned} W_p^p(t_{a\#\mu}, t_{a\#\nu}) &= \inf_{\gamma \in \Pi(\mu, \nu)} \int_{\mathcal{M} \times \mathcal{M}} |t_a(x) - t_a(y)|^p d\gamma(x, y) \\ &\stackrel{(1)}{=} \inf_{\gamma \in \Pi(\tilde{\mu}, \tilde{\nu})} \int_{\mathcal{M} \times \mathcal{M}} |\langle a, \phi(x) \rangle_{\mathcal{E}} - \langle a, \phi(y) \rangle_{\mathcal{E}}|^p d\gamma(x, y) \\ &= W_p^p(\langle \langle a, \cdot \rangle_{\mathcal{E}} \rangle_{\#} \tilde{\mu}, \langle \langle a, \cdot \rangle_{\mathcal{E}} \rangle_{\#} \tilde{\nu}), \end{aligned} \quad (58)$$

where $(\phi \times \phi)_{\#}\gamma \in \Pi(\tilde{\mu}, \tilde{\nu})$.

The derivation of Eq. (58) follows.

(1) follows from Eq. (57), since the constant terms $\langle a, \phi(x_0) \rangle_{\mathcal{E}}$ cancel out in the difference $t_a(x) - t_a(y)$.

By integrating both sides of Eq. (58) with respect to $a \in S_{\mathcal{E}}$, we obtain

$$\text{PEMSW}_p^p(\mu, \nu) = \text{SW}_p^p(\tilde{\mu}, \tilde{\nu}). \quad (59)$$

\square

B.4 Proof of the Prop. 3.5

PROOF OF PROP. 3.5. For any $a \in S_{\mathcal{E}}$, the slicing coordinate associated with x_i is given by

$$t_a^{(x_i)}(x) = \langle a, \phi(x) - \phi(x_i) \rangle_{\mathcal{E}}, \quad i \in \{0, 1\}. \quad (60)$$

Therefore, for all $x \in \mathcal{M}$,

$$t_a^{(x_1)}(x) = t_a^{(x_0)}(x) + \langle a, \phi(x_0) - \phi(x_1) \rangle_{\mathcal{E}}. \quad (61)$$

Hence, there exists a constant $c_a \in \mathbb{R}$ such that

$$t_a^{(x_1)} = \tau_{c_a} \circ t_a^{(x_0)}, \quad (62)$$

where $\tau_{c_a}(s) = s + c_a$ denotes a translation on \mathbb{R} . Consequently,

$$\begin{aligned} t_a^{(x_1)} \# \mu &= (\tau_{c_a}) \# (t_a^{(x_0)} \# \mu), \\ t_a^{(x_1)} \# \nu &= (\tau_{c_a}) \# (t_a^{(x_0)} \# \nu). \end{aligned} \quad (63)$$

Since the p -Wasserstein distance on \mathbb{R} is invariant under translations, it follows that

$$W_p(t_a^{(x_0)} \# \mu, t_a^{(x_0)} \# \nu) = W_p(t_a^{(x_1)} \# \mu, t_a^{(x_1)} \# \nu), \quad \forall a \in S_{\mathcal{E}}. \quad (64)$$

This establishes the reference-point invariance of PEMSW_p . \square

B.5 Proof of the Thm. 3.6

PROOF OF THM. 3.6. Let $p \geq 1$ and let $\mu, \nu \in \mathcal{P}_p(\mathcal{M})$. We verify that PEMSW_p is finite, symmetric, satisfies the triangle inequality, and vanishes if and only if $\mu = \nu$.

(i) **Finiteness.** For any $a \in S_{\mathcal{E}}$, the slicing coordinate is given by

$$t_a(x) = \langle a, \phi(x) - \phi(x_0) \rangle_{\mathcal{E}}, \quad \forall x \in \mathcal{M}. \quad (65)$$

For any $x, y \in \mathcal{M}$, we have

$$\begin{aligned} |t_a(x) - t_a(y)| &= |\langle a, \phi(x) - \phi(x_0) \rangle_{\mathcal{E}} - \langle a, \phi(y) - \phi(x_0) \rangle_{\mathcal{E}}| \\ &= |\langle a, \phi(x) - \phi(y) \rangle_{\mathcal{E}}| \\ &\stackrel{(1)}{\leq} \|a\|_{\mathcal{E}} \|\phi(x) - \phi(y)\|_{\mathcal{E}} \\ &\stackrel{(2)}{=} \|\phi(x) - \phi(y)\|_{\mathcal{E}} \\ &\stackrel{(3)}{=} d_{\mathcal{M}}(x, y). \end{aligned} \quad (66)$$

The derivation of Eq. (66) follows.

(1) follows from the Cauchy–Schwarz inequality in \mathcal{E} .

(2) follows from $a \in S_{\mathcal{E}}$.

(3) follows from the pullback Euclidean distance $d_{\mathcal{M}}(x, y) = \|\phi(x) - \phi(y)\|_{\mathcal{E}}$.

Inequality Eq. (66) shows that $t_a : \mathcal{M} \rightarrow \mathbb{R}$ is 1-Lipschitz. Let $\gamma \in \Pi(\mu, \nu)$ be an arbitrary coupling. Then, following Eq. (66), we can obtain

$$\int_{\mathcal{M} \times \mathcal{M}} |t_a(x) - t_a(y)|^p d\gamma(x, y) \leq \int_{\mathcal{M} \times \mathcal{M}} d_{\mathcal{M}}(x, y)^p d\gamma(x, y). \quad (67)$$

Since $\mu, \nu \in \mathcal{P}_p(\mathcal{M})$, there exists at least one coupling $\gamma \in \Pi(\mu, \nu)$ for which the right-hand side in Eq. (67) is finite. Consequently, the infimum in the definition of $W_p^p(t_a \# \mu, t_a \# \nu)$ is finite, and thus

$$W_p(t_a \# \mu, t_a \# \nu) < \infty, \quad \forall a \in S_{\mathcal{E}}. \quad (68)$$

Finally, $\text{PEMSW}_p(\mu, \nu)$ is obtained by integrating $W_p^p(t_a \# \mu, t_a \# \nu)$ over $a \in S_{\mathcal{E}}$ and taking the p -th root. Since the integrand is finite for every $a \in S_{\mathcal{E}}$, it follows that $\text{PEMSW}_p(\mu, \nu) < \infty$.

(ii) **Symmetry and non-negativity.** For each $a \in S_{\mathcal{E}}$, the one-dimensional Wasserstein distance on \mathbb{R} satisfies

$$W_p(t_a \# \mu, t_a \# \nu) = W_p(t_a \# \nu, t_a \# \mu) \quad \text{and} \quad W_p(t_a \# \mu, t_a \# \nu) \geq 0. \quad (69)$$

Using the integral form of PEMSW_p , we obtain

$$\begin{aligned} \text{PEMSW}_p(\mu, \nu) &= \left(\int_{S_{\mathcal{E}}} W_p^p(t_a \# \mu, t_a \# \nu) d\lambda(a) \right)^{\frac{1}{p}} \\ &= \left(\int_{S_{\mathcal{E}}} W_p^p(t_a \# \nu, t_a \# \mu) d\lambda(a) \right)^{\frac{1}{p}} \\ &= \text{PEMSW}_p(\nu, \mu). \end{aligned} \quad (70)$$

In addition, non-negativity follows directly from the definition of PEMSW_p , since

$$\text{PEMSW}_p(\mu, \nu) = \left(\int_{S_{\mathcal{E}}} W_p^p(t_a \# \mu, t_a \# \nu) d\lambda(a) \right)^{\frac{1}{p}} \geq 0, \quad (71)$$

as the integrand is non-negative for all $a \in S_{\mathcal{E}}$.

(iii) **Triangle inequality.** Let $\alpha \in \mathcal{P}_p(\mathcal{M})$. For each $a \in S_{\mathcal{E}}$, the triangle inequality for the one-dimensional Wasserstein distance yields

$$W_p(t_a \# \mu, t_a \# \nu) \leq W_p(t_a \# \mu, t_a \# \alpha) + W_p(t_a \# \alpha, t_a \# \nu). \quad (72)$$

Using the integral representation of PEMSW_p , we obtain

$$\begin{aligned} \text{PEMSW}_p(\mu, \nu) &= \left(\int_{S_{\mathcal{E}}} W_p^p(t_a \# \mu, t_a \# \nu) d\lambda(a) \right)^{\frac{1}{p}} \\ &\stackrel{(1)}{\leq} \left(\int_{S_{\mathcal{E}}} (W_p(t_a \# \mu, t_a \# \alpha) + W_p(t_a \# \alpha, t_a \# \nu))^p d\lambda(a) \right)^{\frac{1}{p}} \\ &\stackrel{(2)}{\leq} \left(\int_{S_{\mathcal{E}}} W_p^p(t_a \# \mu, t_a \# \alpha) d\lambda(a) \right)^{\frac{1}{p}} + \left(\int_{S_{\mathcal{E}}} W_p^p(t_a \# \alpha, t_a \# \nu) d\lambda(a) \right)^{\frac{1}{p}} \\ &= \text{PEMSW}_p(\mu, \alpha) + \text{PEMSW}_p(\alpha, \nu). \end{aligned} \quad (73)$$

(iv) **Indiscernibility.** Assume that $\text{PEMSW}_p(\mu, \nu) = 0$. By the definition of PEMSW_p , this means that

$$\int_{S_{\mathcal{E}}} W_p^p(t_a \# \mu, t_a \# \nu) d\lambda(a) = 0, \quad (74)$$

where λ denotes the uniform probability measure on $S_{\mathcal{E}}$. Since the integrand in Eq. (74) is non-negative, the integral can vanish only if

$$W_p(t_a \# \mu, t_a \# \nu) = 0 \quad \text{for } \lambda\text{-almost every } a \in S_{\mathcal{E}}. \quad (75)$$

Because W_p is a distance on \mathbb{R} , Eq. (75) is equivalent to

$$t_a \# \mu = t_a \# \nu \quad \text{for } \lambda\text{-almost every } a \in S_{\mathcal{E}}. \quad (76)$$

Next, we make use of the translation representation in Lem. 3.3, which gives

$$t_a(x) = \langle a, \phi(x) \rangle_{\mathcal{E}} - \langle a, \phi(x_0) \rangle_{\mathcal{E}}, \quad \forall x \in \mathcal{M}. \quad (77)$$

As a consequence, $t_a \# \mu$ is obtained from $(\langle a, \cdot \rangle_{\mathcal{E}}) \# (\phi \# \mu)$ by a translation on \mathbb{R} , and the same holds for ν . Since translations preserve equality of probability measures on \mathbb{R} , Eq. (76) implies

$$(\langle a, \cdot \rangle_{\mathcal{E}}) \# (\phi \# \mu) = (\langle a, \cdot \rangle_{\mathcal{E}}) \# (\phi \# \nu) \quad \text{for } \lambda\text{-almost every } a \in S_{\mathcal{E}}. \quad (78)$$

The collection of linear functionals $\{\langle a, \cdot \rangle_{\mathcal{E}}\}_{a \in S_{\mathcal{E}}}$ separates probability measures on the Euclidean space \mathcal{E} . Therefore, Eq. (78) yields

$$\phi_{\#}\mu = \phi_{\#}\nu. \quad (79)$$

Finally, since ϕ is bijective, the equality above implies $\mu = \nu$.

Conversely, if $\mu = \nu$, then $t_{a\#}\mu = t_{a\#}\nu$ holds for every $a \in S_{\mathcal{E}}$, and hence $W_p(t_{a\#}\mu, t_{a\#}\nu) = 0$. Integrating over $a \in S_{\mathcal{E}}$ shows that $\text{PEMSW}_p(\mu, \nu) = 0$.

Therefore, $\text{PEMSW}_p(\mu, \nu) = 0$ if and only if $\mu = \nu$. \square

B.6 Proof of the Thm. 3.7

PROOF OF THM. 3.7. Let $p \geq 1$ and let $\mu \in \mathcal{P}_p(\mathcal{M})$. Consider a sequence $(\mu_k)_k \subset \mathcal{P}_p(\mathcal{M})$. The proof relies on the reduction of PEMSW_p to the Euclidean sliced Wasserstein distance through the pullback embedding ϕ .

(\Rightarrow) Weak convergence implies vanishing PEMSW_p . Suppose that $\mu_k \rightarrow \mu$ in $\mathcal{P}_p(\mathcal{M})$. Since $\phi : \mathcal{M} \rightarrow \mathcal{E}$ is continuous, the continuous mapping theorem yields

$$\phi_{\#}\mu_k \rightarrow \phi_{\#}\mu \quad \text{in } \mathcal{P}(\mathcal{E}). \quad (80)$$

Next, we verify that the p -moments of the pushforward measures also converge. Fix an arbitrary point $z_0 \in \mathcal{E}$ and set $x_0 = \phi^{-1}(z_0) \in \mathcal{M}$. Then we have

$$\begin{aligned} \int_{\mathcal{E}} \|z - z_0\|_{\mathcal{E}}^p d(\phi_{\#}\mu_k)(z) &\stackrel{(1)}{=} \int_{\mathcal{M}} \|\phi(x) - z_0\|_{\mathcal{E}}^p d\mu_k(x) \\ &= \int_{\mathcal{M}} \|\phi(x) - \phi(x_0)\|_{\mathcal{E}}^p d\mu_k(x) \quad (81) \\ &\stackrel{(2)}{=} \int_{\mathcal{M}} d_{\mathcal{M}}(x, x_0)^p d\mu_k(x), \end{aligned}$$

and the same identity holds with μ_k replaced by μ .

The derivation of Eq. (81) follows.

(1) follows from the definition of pushforward measures.

(2) follows from the pullback Euclidean distance $d_{\mathcal{M}}(x, y) = \|\phi(x) - \phi(y)\|_{\mathcal{E}}$.

Since $\mu_k \rightarrow \mu$ in $\mathcal{P}_p(\mathcal{M})$, we have

$$\int_{\mathcal{M}} d_{\mathcal{M}}(x, x_0)^p d\mu_k(x) \rightarrow \int_{\mathcal{M}} d_{\mathcal{M}}(x, x_0)^p d\mu(x), \quad (82)$$

and combining Eqs. (81) and (82) yields

$$\int_{\mathcal{E}} \|z - z_0\|_{\mathcal{E}}^p d(\phi_{\#}\mu_k)(z) \rightarrow \int_{\mathcal{E}} \|z - z_0\|_{\mathcal{E}}^p d(\phi_{\#}\mu)(z). \quad (83)$$

Therefore, Eqs. (80) and (83) show that $\phi_{\#}\mu_k \rightarrow \phi_{\#}\mu$ in W_p on \mathcal{E} , i.e.,

$$W_p(\phi_{\#}\mu_k, \phi_{\#}\mu) \rightarrow 0. \quad (84)$$

Finally, we translate Eq. (84) back to PEMSW_p . By Thm. 3.4, the identity $\text{PEMSW}_p(\mu_k, \mu) = \text{SW}_p(\phi_{\#}\mu_k, \phi_{\#}\mu)$ holds, and hence

$$\text{PEMSW}_p(\mu_k, \mu) = \text{SW}_p(\phi_{\#}\mu_k, \phi_{\#}\mu) \rightarrow 0. \quad (85)$$

(\Leftarrow) Vanishing PEMSW_p implies weak convergence. We now consider the case where the sequence $(\mu_k)_k$ satisfies

$$\text{PEMSW}_p(\mu_k, \mu) \rightarrow 0. \quad (86)$$

By the equivalence between PEMSW_p and the Euclidean sliced Wasserstein distance established in Thm. 3.4, the convergence in Eq. (86) is equivalent to

$$\text{SW}_p(\phi_{\#}\mu_k, \phi_{\#}\mu) \rightarrow 0. \quad (87)$$

At this stage, the analysis can be carried out entirely in the Euclidean space \mathcal{E} . It is a standard result that the sliced Wasserstein distance SW_p metrizes weak convergence on $\mathcal{P}_p(\mathcal{E})$. Consequently, the convergence in Eq. (87) implies

$$\phi_{\#}\mu_k \rightarrow \phi_{\#}\mu \quad \text{in } \mathcal{P}_p(\mathcal{E}), \quad (88)$$

that is, the pushforward measures converge weakly in the embedding space.

We next transfer the convergence in Eq. (88) back to the manifold \mathcal{M} . Let $f \in C_b(\mathcal{M})$ be an arbitrary bounded continuous test function. Since ϕ is a homeomorphism between \mathcal{M} and its image $\phi(\mathcal{M}) \subset \mathcal{E}$, the composition $f \circ \phi^{-1}$ belongs to $C_b(\mathcal{E})$. Therefore, the weak convergence of the pushforward measures yields

$$\begin{aligned} \int_{\mathcal{M}} f(x) d\mu_k(x) &= \int_{\mathcal{E}} f(\phi^{-1}(z)) d(\phi_{\#}\mu_k)(z) \\ &\rightarrow \int_{\mathcal{E}} f(\phi^{-1}(z)) d(\phi_{\#}\mu)(z) \quad (89) \\ &= \int_{\mathcal{M}} f(x) d\mu(x). \end{aligned}$$

Since Eq. (89) holds for all $f \in C_b(\mathcal{M})$, this establishes the weak convergence

$$\mu_k \rightarrow \mu \quad \text{in } \mathcal{P}_p(\mathcal{M}). \quad (90)$$

Combining the two directions completes the proof. \square

B.7 Proof of the Prop. 3.8

This subsection proves an upper comparison between PEMSW_p and the full Wasserstein distance on \mathcal{M} . The proof uses two facts repeatedly: the pullback identity from Thm. 3.4 and the rotational invariance of the uniform measure on $S_{\mathcal{E}}$.

Lemma B.4 (Spherical averaging of one-dimensional projections). *Let $D = \dim(\mathcal{E})$ and let λ be the uniform probability measure on $S_{\mathcal{E}}$. For any $v \in \mathcal{E}$ and any $p \geq 1$, the spherical average satisfies*

$$\int_{S_{\mathcal{E}}} |\langle a, v \rangle_{\mathcal{E}}|^p d\lambda(a) = \kappa_{D,p} \|v\|_{\mathcal{E}}^p, \quad \kappa_{D,p} = \int_{S^{D-1}} |\theta_1|^p d\lambda(\theta). \quad (91)$$

In particular, the case $p = 2$ yields $\kappa_{D,2} = 1/D$.

PROOF OF LEM. B.4. The integral on the left-hand side of Eq. (91) is invariant under orthogonal transformations of \mathcal{E} because λ is rotation invariant on $S_{\mathcal{E}}$. This invariance implies that the integral depends on v only through $\|v\|_{\mathcal{E}}$, so the integral must equal $c_{D,p} \|v\|_{\mathcal{E}}^p$ for some constant $c_{D,p}$. To identify the constant, the proof chooses an orthonormal basis of \mathcal{E} such that $v = \|v\|_{\mathcal{E}} e_1$. This choice gives

$$\int_{S_{\mathcal{E}}} |\langle a, v \rangle_{\mathcal{E}}|^p d\lambda(a) = \|v\|_{\mathcal{E}}^p \int_{S_{\mathcal{E}}} |\langle a, e_1 \rangle_{\mathcal{E}}|^p d\lambda(a) = \kappa_{D,p} \|v\|_{\mathcal{E}}^p, \quad (92)$$

which establishes Eq. (91). The identity $\kappa_{D,2} = 1/D$ follows from symmetry and the constraint $\sum_{i=1}^D \theta_i^2 = 1$ on S^{D-1} . \square

PROOF OF PROP. 3.8. Let $p \geq 1$ and let $\mu, \nu \in \mathcal{P}_p(\mathcal{M})$. The proof introduces the embedded measures $\tilde{\mu} = \phi_{\#}\mu$ and $\tilde{\nu} = \phi_{\#}\nu$ in \mathcal{E} . The pullback framework in Thm. 3.4 provides the identities

$$\text{PEMSW}_p(\mu, \nu) = \text{SW}_p(\tilde{\mu}, \tilde{\nu}) \quad \text{and} \quad W_p^M(\mu, \nu) = W_p(\tilde{\mu}, \tilde{\nu}). \quad (93)$$

The proof therefore bounds $\text{SW}_p(\tilde{\mu}, \tilde{\nu})$ by $W_p(\tilde{\mu}, \tilde{\nu})$ in \mathcal{E} .

The proof fixes an optimal coupling $\tilde{\gamma}^* \in \Pi(\tilde{\mu}, \tilde{\nu})$ for $W_p(\tilde{\mu}, \tilde{\nu})$. The proof also recalls that each direction $a \in S_{\mathcal{E}}$ defines a linear projection $\pi_a : \mathcal{E} \rightarrow \mathbb{R}$ by $\pi_a(z) = \langle a, z \rangle_{\mathcal{E}}$. For each such a , the definition of W_p yields the coupling upper bound

$$\begin{aligned} W_p(\pi_{a\#}\tilde{\mu}, \pi_{a\#}\tilde{\nu})^p &\leq \int_{\mathcal{E} \times \mathcal{E}} |\pi_a(z) - \pi_a(w)|^p d\tilde{\gamma}^*(z, w) \\ &\stackrel{(1)}{=} \int_{\mathcal{E} \times \mathcal{E}} |\langle a, z - w \rangle_{\mathcal{E}}|^p d\tilde{\gamma}^*(z, w). \end{aligned} \quad (94)$$

The derivation of Eq. (94) follows.

(1) follows from the linearity of π_a .

The proof integrates Eq. (94) over $a \in S_{\mathcal{E}}$ and uses Fubini's theorem to exchange the order of integration:

$$\begin{aligned} \text{SW}_p(\tilde{\mu}, \tilde{\nu})^p &= \int_{S_{\mathcal{E}}} W_p(\pi_{a\#}\tilde{\mu}, \pi_{a\#}\tilde{\nu})^p d\lambda(a) \\ &\leq \int_{\mathcal{E} \times \mathcal{E}} \left(\int_{S_{\mathcal{E}}} |\langle a, z - w \rangle_{\mathcal{E}}|^p d\lambda(a) \right) d\tilde{\gamma}^*(z, w). \end{aligned} \quad (95)$$

Lemma B.4 evaluates the inner spherical integral with $v = z - w$:

$$\int_{S_{\mathcal{E}}} |\langle a, z - w \rangle_{\mathcal{E}}|^p d\lambda(a) = \kappa_{D,p} \|z - w\|_{\mathcal{E}}^p. \quad (96)$$

The proof substitutes this identity into Eq. (95) and obtains

$$\text{SW}_p(\tilde{\mu}, \tilde{\nu})^p \leq \kappa_{D,p} \int_{\mathcal{E} \times \mathcal{E}} \|z - w\|_{\mathcal{E}}^p d\tilde{\gamma}^*(z, w) = \kappa_{D,p} W_p(\tilde{\mu}, \tilde{\nu})^p. \quad (97)$$

The identities in Eq. (93) transfer Eq. (97) back to \mathcal{M} and yield

$$\text{PEMSW}_p(\mu, \nu)^p \leq \kappa_{D,p} W_p^M(\mu, \nu)^p. \quad (98)$$

The special case $p = 2$ follows from $\kappa_{D,2} = 1/D$ in Lemma B.4. \square

B.8 Proof of the Prop. 3.9

This subsection derives a lower bound on PEMSW_p in terms of the difference between the Euclidean means of the embedded measures. The proof first bounds each one-dimensional Wasserstein term from below by the difference of one-dimensional means and then averages the result over $S_{\mathcal{E}}$.

PROOF OF PROP. 3.9. Let $p \geq 1$ and let $\mu, \nu \in \mathcal{P}_p(\mathcal{M})$. The proof again uses $\tilde{\mu} = \phi_{\#}\mu$ and $\tilde{\nu} = \phi_{\#}\nu$. The proof also fixes $a \in S_{\mathcal{E}}$ and applies a Jensen-type bound to any coupling $\gamma \in \Pi(\mu, \nu)$:

$$\int_{\mathcal{M} \times \mathcal{M}} |t_a(x) - t_a(y)|^p d\gamma(x, y) \geq \left| \int_{\mathcal{M} \times \mathcal{M}} (t_a(x) - t_a(y)) d\gamma(x, y) \right|^p. \quad (99)$$

The infimum over $\gamma \in \Pi(\mu, \nu)$ turns Eq. (99) into a pointwise lower bound for W_p :

$$W_p(t_{a\#}\mu, t_{a\#}\nu)^p \geq \left| \int_{\mathcal{M}} t_a(x) d\mu(x) - \int_{\mathcal{M}} t_a(y) d\nu(y) \right|^p. \quad (100)$$

The slicing coordinate formula in Eq. (12) expresses t_a as $t_a(x) = \langle a, \phi(x) - \phi(x_0) \rangle_{\mathcal{E}}$. This representation implies that the reference

term cancels in the difference of expectations, and the proof obtains

$$\begin{aligned} \int_{\mathcal{M}} t_a(x) d\mu(x) - \int_{\mathcal{M}} t_a(y) d\nu(y) &= \left\langle a, \int_{\mathcal{M}} \phi(x) d\mu(x) - \int_{\mathcal{M}} \phi(y) d\nu(y) \right\rangle_{\mathcal{E}} \\ &= \langle a, m_{\tilde{\mu}} - m_{\tilde{\nu}} \rangle_{\mathcal{E}}, \end{aligned} \quad (101)$$

where $m_{\tilde{\mu}} = \int_{\mathcal{E}} z d\tilde{\mu}(z)$ and $m_{\tilde{\nu}} = \int_{\mathcal{E}} z d\tilde{\nu}(z)$. The combination of Eqs. (100) and (101) yields

$$W_p(t_{a\#}\mu, t_{a\#}\nu)^p \geq |\langle a, m_{\tilde{\mu}} - m_{\tilde{\nu}} \rangle_{\mathcal{E}}|^p. \quad (102)$$

The definition of PEMSW_p integrates $W_p^p(t_{a\#}\mu, t_{a\#}\nu)$ over $S_{\mathcal{E}}$. This definition and Eq. (102) yield

$$\text{PEMSW}_p(\mu, \nu)^p \geq \int_{S_{\mathcal{E}}} |\langle a, m_{\tilde{\mu}} - m_{\tilde{\nu}} \rangle_{\mathcal{E}}|^p d\lambda(a). \quad (103)$$

Lemma B.4 evaluates the remaining spherical integral and gives

$$\int_{S_{\mathcal{E}}} |\langle a, m_{\tilde{\mu}} - m_{\tilde{\nu}} \rangle_{\mathcal{E}}|^p d\lambda(a) = \kappa_{D,p} \|m_{\tilde{\mu}} - m_{\tilde{\nu}}\|_{\mathcal{E}}^p. \quad (104)$$

The last identity and Eq. (103) establish Eq. (21). \square

B.9 Proof of the Prop. 3.10

This subsection proves the two-sided comparison between PEMSW_p , the max-sliced variant, and W_p^M . The first inequality compares an L^p -average with a supremum, while the second inequality uses a 1-Lipschitz control of the slicing maps.

PROOF OF PROP. 3.10. Let $p \geq 1$ and let $\mu, \nu \in \mathcal{P}_p(\mathcal{M})$.

(i) The proof shows that $\text{PEMSW}_p(\mu, \nu) \leq \text{PEM-MaxSW}_p(\mu, \nu)$. The definition of the supremum implies that every direction $a \in S_{\mathcal{E}}$ satisfies

$$W_p(t_{a\#}\mu, t_{a\#}\nu) \leq \sup_{b \in S_{\mathcal{E}}} W_p(t_{b\#}\mu, t_{b\#}\nu). \quad (105)$$

The proof raises both sides to the power p and integrates with respect to λ :

$$\int_{S_{\mathcal{E}}} W_p(t_{a\#}\mu, t_{a\#}\nu)^p d\lambda(a) \leq \int_{S_{\mathcal{E}}} \left(\sup_{b \in S_{\mathcal{E}}} W_p(t_{b\#}\mu, t_{b\#}\nu) \right)^p d\lambda(a). \quad (106)$$

Because λ is a probability measure, the integral on the right-hand side equals the constant $\left(\sup_{b \in S_{\mathcal{E}}} W_p(t_{b\#}\mu, t_{b\#}\nu) \right)^p$. The definition of PEMSW_p completes the first inequality:

$$\text{PEMSW}_p(\mu, \nu) \leq \sup_{a \in S_{\mathcal{E}}} W_p(t_{a\#}\mu, t_{a\#}\nu) = \text{PEM-MaxSW}_p(\mu, \nu). \quad (107)$$

(ii) The proof shows that $\text{PEM-MaxSW}_p(\mu, \nu) \leq W_p^M(\mu, \nu)$. The proof fixes $a \in S_{\mathcal{E}}$ and chooses an optimal coupling $\gamma^* \in \Pi(\mu, \nu)$ for $W_p^M(\mu, \nu)$. The definition of W_p gives

$$W_p(t_{a\#}\mu, t_{a\#}\nu)^p \leq \int_{\mathcal{M} \times \mathcal{M}} |t_a(x) - t_a(y)|^p d\gamma^*(x, y). \quad (108)$$

The proof rewrites the integrand by using Eq. (12) and cancellation of the reference term:

$$|t_a(x) - t_a(y)| = |\langle a, \phi(x) - \phi(y) \rangle_{\mathcal{E}}|. \quad (109)$$

Cauchy–Schwarz and $\|a\|_{\mathcal{E}} = 1$ yield the pointwise estimate

$$|\langle a, \phi(x) - \phi(y) \rangle_{\mathcal{E}}| \leq \|\phi(x) - \phi(y)\|_{\mathcal{E}}. \quad (110)$$

The pullback Euclidean identity $d_{\mathcal{M}}(x, y) = \|\phi(x) - \phi(y)\|_{\mathcal{E}}$ therefore yields

$$W_p(t_{a\#}\mu, t_{a\#}\nu)^p \leq \int_{\mathcal{M} \times \mathcal{M}} d_{\mathcal{M}}(x, y)^p d\gamma^*(x, y) = W_p^{\mathcal{M}}(\mu, \nu)^p. \quad (111)$$

The proof finishes by taking the supremum over $a \in S_{\mathcal{E}}$ and combining the two steps. \square

B.10 Proof of the Thm. 3.11

This subsection proves a reverse inequality under compact support in the embedding space. The proof first reduces the statement to an inequality in \mathcal{E} via Thm. 3.4. The proof then combines three ingredients: a bounded-support comparison between W_p and W_1 , a reverse inequality relating W_1 to SW_1 , and a final conversion from SW_1 to SW_p .

PROOF OF THM. 3.11. Let $p \geq 1$ and fix $R > 0$. Let $\mu, \nu \in \mathcal{P}_p(\mathcal{M}_R)$ and define $\tilde{\mu} = \phi_{\#}\mu$ and $\tilde{\nu} = \phi_{\#}\nu$. The definition of \mathcal{M}_R implies that both embedded measures satisfy

$$\text{supp}(\tilde{\mu}) \cup \text{supp}(\tilde{\nu}) \subset B_{\mathcal{E}}(\phi(x_0), R). \quad (112)$$

The pullback identities in Thm. 3.4 convert the target inequality on \mathcal{M} into an inequality on \mathcal{E} :

$$W_p^{\mathcal{M}}(\mu, \nu) = W_p(\tilde{\mu}, \tilde{\nu}), \quad \text{PEMSW}_p(\mu, \nu) = \text{SW}_p(\tilde{\mu}, \tilde{\nu}). \quad (113)$$

Step 1: The proof bounds $W_p(\tilde{\mu}, \tilde{\nu})$ by $W_1(\tilde{\mu}, \tilde{\nu})$ on a bounded set. Every pair (z, w) in $B_{\mathcal{E}}(\phi(x_0), R)$ satisfies $\|z - w\|_{\mathcal{E}} \leq 2R$. The scalar inequality $\rho^p \leq (2R)^{p-1}\rho$ for $\rho \in [0, 2R]$ therefore yields, for every coupling $\tilde{\gamma} \in \Pi(\tilde{\mu}, \tilde{\nu})$,

$$\int_{\mathcal{E} \times \mathcal{E}} \|z - w\|_{\mathcal{E}}^p d\tilde{\gamma}(z, w) \leq (2R)^{p-1} \int_{\mathcal{E} \times \mathcal{E}} \|z - w\|_{\mathcal{E}} d\tilde{\gamma}(z, w). \quad (114)$$

The infimum over $\tilde{\gamma} \in \Pi(\tilde{\mu}, \tilde{\nu})$ yields

$$W_p(\tilde{\mu}, \tilde{\nu})^p \leq (2R)^{p-1} W_1(\tilde{\mu}, \tilde{\nu}). \quad (115)$$

Step 2: The proof bounds $W_1(\tilde{\mu}, \tilde{\nu})$ by $SW_1(\tilde{\mu}, \tilde{\nu})$ under compact support. A reverse inequality for Euclidean sliced Wasserstein distances with bounded support (see, e.g., [16, Theorem 5.1.5]) ensures that a constant $C_{D,R} > 0$ exists such that

$$W_1(\tilde{\mu}, \tilde{\nu}) \leq C_{D,R} SW_1(\tilde{\mu}, \tilde{\nu})^{\frac{2}{D+2}}. \quad (116)$$

Step 3: The proof replaces SW_1 by SW_p and adjusts the exponent. Hölder's inequality on the probability space $(S_{\mathcal{E}}, \lambda)$ yields

$$SW_1(\tilde{\mu}, \tilde{\nu}) \leq SW_p(\tilde{\mu}, \tilde{\nu}). \quad (117)$$

The compact support also bounds the magnitude of the sliced distance because the upper comparison in Prop. 3.8 gives

$$SW_p(\tilde{\mu}, \tilde{\nu}) \leq W_p(\tilde{\mu}, \tilde{\nu}) \leq 2R. \quad (118)$$

The proof combines $\alpha = \frac{2}{D+2}$ and $\beta = \frac{1}{D+1}$ and uses $\alpha > \beta$ together with Eq. (118). This combination yields the inequality

$$SW_p(\tilde{\mu}, \tilde{\nu})^{\alpha} = SW_p(\tilde{\mu}, \tilde{\nu})^{\beta} SW_p(\tilde{\mu}, \tilde{\nu})^{\alpha-\beta} \leq (2R)^{\alpha-\beta} SW_p(\tilde{\mu}, \tilde{\nu})^{\beta}. \quad (119)$$

Step 4: The proof combines the bounds and transfers the result to \mathcal{M} . The inequalities Eqs. (115) to (117) and (119) yield

$$W_p(\tilde{\mu}, \tilde{\nu})^p \leq (2R)^{p-1} C_{D,R} (2R)^{\alpha-\beta} SW_p(\tilde{\mu}, \tilde{\nu})^{\beta}. \quad (120)$$

The proof absorbs the constants into a single quantity $C_{D,p,R} > 0$ and obtains

$$W_p(\tilde{\mu}, \tilde{\nu})^p \leq C_{D,p,R} SW_p(\tilde{\mu}, \tilde{\nu})^{\frac{1}{D+1}}. \quad (121)$$

The identities in Eq. (113) convert Eq. (121) into the desired bound on \mathcal{M} :

$$W_p^{\mathcal{M}}(\mu, \nu)^p \leq C_{D,p,R} \text{PEMSW}_p(\mu, \nu)^{\frac{1}{D+1}}. \quad (122)$$

This inequality completes the proof. \square

B.11 Proof of the Prop. 3.12

This subsection establishes a plug-in stability bound for PEMSW_p when both input measures are replaced by empirical measures. The proof separates the statistical error into two one-sample terms and controls each term by reducing the problem to one-dimensional Wasserstein deviations along pullback slicing directions. The argument finally relates the one-dimensional moments to the q -th moment of the embedded measures in \mathcal{E} .

Lemma B.5 (One-dimensional empirical Wasserstein rate on \mathbb{R}). *Let $p \geq 1$ and let $\eta \in \mathcal{P}_p(\mathbb{R})$ satisfy $M_q(\eta) = \int_{\mathbb{R}} |u|^q d\eta(u) < \infty$ for some $q > p$. Let $\hat{\eta}_n$ be the empirical measure built from n i.i.d. samples from η . There exists a constant $C_{p,q} > 0$, depending only on (p, q) , such that*

$$\mathbb{E} \left[W_p^p(\hat{\eta}_n, \eta) \right] \leq C_{p,q} M_q(\eta)^{p/q} \beta_{n,p,q}, \quad (123)$$

where

$$\beta_{n,p,q} = \begin{cases} n^{-1/2} & \text{if } q > 2p, \\ n^{-1/2} \log(n) & \text{if } q = 2p, \\ n^{-(q-p)/q} & \text{if } q \in (p, 2p). \end{cases} \quad (124)$$

PROOF. Lemma B.5 is a direct specialization to \mathbb{R} of the empirical Wasserstein rates proved in Fournier and Guillin [38], and the stated form can be found, for example, in Rakotomamonjy et al. [70, Lemma 1]. \square

PROOF OF PROP. 3.12. Let $q > p \geq 1$ and let $\mu, \nu \in \mathcal{P}_q(\mathcal{M})$. Let $\hat{\mu}_n$ and $\hat{\nu}_n$ be empirical measures built from n i.i.d. samples from μ and ν . The proof uses the triangle inequality of PEMSW_p in the space $\mathcal{P}_p(\mathcal{M})$:

$$\left| \text{PEMSW}_p(\hat{\mu}_n, \hat{\nu}_n) - \text{PEMSW}_p(\mu, \nu) \right| \leq \text{PEMSW}_p(\hat{\mu}_n, \mu) + \text{PEMSW}_p(\hat{\nu}_n, \nu). \quad (125)$$

Taking expectations in Eq. (125) yields

$$\mathbb{E} \left[\left| \text{PEMSW}_p(\hat{\mu}_n, \hat{\nu}_n) - \text{PEMSW}_p(\mu, \nu) \right| \right] \leq \mathbb{E} \left[\text{PEMSW}_p(\hat{\mu}_n, \mu) \right] + \mathbb{E} \left[\text{PEMSW}_p(\hat{\nu}_n, \nu) \right]. \quad (126)$$

The definition of PEMSW_p and the concavity of $x \mapsto x^{1/p}$ imply a Jensen-type bound. This bound gives, for any random nonnegative variable X , $\mathbb{E}[X^{1/p}] \leq \mathbb{E}[X]^{1/p}$. Applying this inequality with $X = \int_{S_{\mathcal{E}}} W_p^p(t_{a\#}\hat{\mu}_n, t_{a\#}\mu) d\lambda(a)$ yields

$$\mathbb{E} \left[\text{PEMSW}_p(\hat{\mu}_n, \mu) \right] \leq \left(\mathbb{E} \left[\int_{S_{\mathcal{E}}} W_p^p(t_{a\#}\hat{\mu}_n, t_{a\#}\mu) d\lambda(a) \right] \right)^{1/p}. \quad (127)$$

Fubini–Tonelli justifies the exchange of expectation and spherical integration in Eq. (127):

$$\mathbb{E} \left[\int_{S_{\mathcal{E}}} W_p^p(t_{a\#}\hat{\mu}_n, t_{a\#}\mu) d\lambda(a) \right] = \int_{S_{\mathcal{E}}} \mathbb{E} \left[W_p^p(t_{a\#}\hat{\mu}_n, t_{a\#}\mu) \right] d\lambda(a). \quad (128)$$

The proof now controls the integrand in Eq. (128) using the one-dimensional rate in Lemma B.5. For each fixed $a \in S_{\mathcal{E}}$, the measure $t_{a\#\mu}$ lies in $\mathcal{P}_q(\mathbb{R})$ because $q > p$ and t_a has at most linear growth in the embedding space. Lemma B.5 applied to $\eta = t_{a\#\mu}$ yields

$$\mathbb{E} \left[W_p^p(t_{a\#\hat{\mu}_n}, t_{a\#\mu}) \right] \leq C_{p,q} M_q(t_{a\#\mu})^{p/q} \beta_{n,p,q}. \quad (129)$$

The remaining task is to control $M_q(t_{a\#\mu})$ uniformly in a through the embedded moment $M_q(\tilde{\mu})$ stated in the proposition. The translation form of t_a in Lem. 3.3 yields $t_a(x) = \langle a, \phi(x) \rangle_{\mathcal{E}} - \langle a, \phi(x_0) \rangle_{\mathcal{E}}$. This identity implies the bound

$$|t_a(x)| = |\langle a, \phi(x) - \phi(x_0) \rangle_{\mathcal{E}}| \leq \|\phi(x) - \phi(x_0)\|_{\mathcal{E}}, \quad (130)$$

which holds because $\|a\|_{\mathcal{E}} = 1$. Using Eq. (130), the q -th moment of $t_{a\#\mu}$ satisfies

$$\begin{aligned} M_q(t_{a\#\mu}) &= \int_{\mathbb{R}} |u|^q d(t_{a\#\mu})(u) \\ &= \int_{\mathcal{M}} |t_a(x)|^q d\mu(x) \\ &\leq \int_{\mathcal{M}} \|\phi(x) - \phi(x_0)\|_{\mathcal{E}}^q d\mu(x) \\ &= \int_{\mathcal{E}} \|z - \phi(x_0)\|_{\mathcal{E}}^q d\tilde{\mu}(z) = M_q(\tilde{\mu}). \end{aligned} \quad (131)$$

The bound Eq. (131) implies $M_q(t_{a\#\mu})^{p/q} \leq M_q(\tilde{\mu})^{p/q}$, uniformly over a . Substituting this uniform control into Eq. (129) and integrating over $S_{\mathcal{E}}$ yields

$$\int_{S_{\mathcal{E}}} \mathbb{E} \left[W_p^p(t_{a\#\hat{\mu}_n}, t_{a\#\mu}) \right] d\lambda(a) \leq C_{p,q} M_q(\tilde{\mu})^{p/q} \beta_{n,p,q}. \quad (132)$$

The combination of Eqs. (127), (128) and (132) gives

$$\mathbb{E} [\text{PEMSW}_p(\hat{\mu}_n, \mu)] \leq C_{p,q}^{1/p} M_q(\tilde{\mu})^{1/q} \beta_{n,p,q}^{1/p}. \quad (133)$$

The same argument with ν yields

$$\mathbb{E} [\text{PEMSW}_p(\hat{\nu}_n, \nu)] \leq C_{p,q}^{1/p} M_q(\tilde{\nu})^{1/q} \beta_{n,p,q}^{1/p}. \quad (134)$$

The proof now rewrites the factor $\beta_{n,p,q}^{1/p}$ as $\alpha_{n,p,q}$ used in the statement:

$$\alpha_{n,p,q} = \beta_{n,p,q}^{1/p} = \begin{cases} n^{-1/(2p)} & \text{if } q > 2p, \\ n^{-1/(2p)} \log(n)^{1/p} & \text{if } q = 2p, \\ n^{-(q-p)/(pq)} & \text{if } q \in (p, 2p). \end{cases} \quad (135)$$

Finally, the definition $M_q(\tilde{\mu}, \tilde{\nu}) = M_q(\tilde{\mu})^{1/q} + M_q(\tilde{\nu})^{1/q}$ combines Eqs. (126) and (133) to (135) into

$$\mathbb{E} \left[\left| \text{PEMSW}_p(\hat{\mu}_n, \hat{\nu}_n) - \text{PEMSW}_p(\mu, \nu) \right| \right] \leq \alpha_{n,p,q} C_{p,q}^{1/p} M_q(\tilde{\mu}, \tilde{\nu}), \quad (136)$$

which completes the proof. \square

B.12 Proof of the Prop. 3.13

This subsection controls the Monte-Carlo error induced by replacing the spherical integral in PEMSW_p^p by an empirical average over L random directions. The proof treats the quantity $W_p^p(t_{a\#\mu}, t_{a\#\nu})$ as a square-integrable random variable of $a \sim \lambda_{\mathcal{E}}$ and applies the classical variance identity for sample means.

PROOF OF PROP. 3.13. Let $p \geq 1$ and let $\mu, \nu \in \mathcal{P}_p(\mathcal{M})$. Let $(a_i)_{i=1}^L$ be i.i.d. random directions drawn from $\lambda_{\mathcal{E}}$ on $S_{\mathcal{E}}$. The proof introduces the random variable

$$Z(a) = W_p^p(t_{a\#\mu}, t_{a\#\nu}), \quad a \sim \lambda_{\mathcal{E}}. \quad (137)$$

The definition of PEMSW_p^p implies that the expectation of $Z(a)$ equals the spherical integral:

$$\mathbb{E}_{a \sim \lambda_{\mathcal{E}}} [Z(a)] = \int_{S_{\mathcal{E}}} W_p^p(t_{a\#\mu}, t_{a\#\nu}) d\lambda_{\mathcal{E}}(a) = \text{PEMSW}_p^p(\mu, \nu). \quad (138)$$

The Monte-Carlo estimator in the proposition is the empirical mean of $Z(a)$:

$$\widehat{\text{PEMSW}}_{p,L}^p(\mu, \nu) = \frac{1}{L} \sum_{i=1}^L Z(a_i). \quad (139)$$

The proof now uses the variance formula for the mean of i.i.d. square-integrable variables. Because $(Z(a_i))_{i=1}^L$ are i.i.d. with variance $\text{Var}(Z(a))$, the estimator satisfies

$$\begin{aligned} \mathbb{E} \left[\left| \widehat{\text{PEMSW}}_{p,L}^p(\mu, \nu) - \text{PEMSW}_p^p(\mu, \nu) \right|^2 \right] \\ = \text{Var} \left(\frac{1}{L} \sum_{i=1}^L Z(a_i) \right) = \frac{1}{L} \text{Var}_{a \sim \lambda_{\mathcal{E}}} [Z(a)]. \end{aligned} \quad (140)$$

The identity Eq. (140) matches the bound stated in Prop. 3.13 and completes the proof. \square

B.13 Proof of the Cor. 3.14

PROOF OF COR. 3.14. The slicing coordinate in Eq. (12) states that, for any $x \in \mathcal{M}$ and any unit direction $a \in S_{\mathcal{E}}$,

$$t_a(x) = \langle a, \phi(x) - \phi(x_0) \rangle_{\mathcal{E}}. \quad (141)$$

In the present setting, the embedding space \mathcal{E} is identified with the OLM tangent-type space equipped with the Frobenius inner product, so $\langle \cdot, \cdot \rangle_{\mathcal{E}} = \langle \cdot, \cdot \rangle_F$ and a is written as $A \in S_{\text{Hol}}$. Substituting $\phi = \text{Log}^{\circ}$, $x = C$, and $x_0 = I_n$ into Eq. (141) gives

$$t_A^{\circ}(C) = \langle A, \text{Log}^{\circ}(C) - \text{Log}^{\circ}(I_n) \rangle_F. \quad (142)$$

The construction of Log° ensures $\text{Log}^{\circ}(I_n) = 0$, and therefore the coordinate reduces to

$$t_A^{\circ}(C) = \langle A, \text{Log}^{\circ}(C) \rangle_F, \quad (143)$$

which is exactly Eq. (32). \square

B.14 Proof of the Cor. 3.16

PROOF OF COR. 3.16. The same specialization of Eq. (12) yields

$$t_A^{\star}(C) = \langle A, \text{Log}^{\star}(C) - \text{Log}^{\star}(I_n) \rangle_F, \quad (144)$$

because the LSM embedding space also uses the Frobenius inner product and the unit direction is written as $A \in S_{\text{Row}}$. The definition of Log^{\star} satisfies $\text{Log}^{\star}(I_n) = 0$, so Eq. (144) simplifies to

$$t_A^{\star}(C) = \langle A, \text{Log}^{\star}(C) \rangle_F, \quad (145)$$

which matches Eq. (34). \square

B.15 Proof of the Prop. 3.18

PROOF OF PROP. 3.18. Let $p \geq 1$ and let $\mu, \nu \in \mathcal{P}_p(S_d^{++})$. The proof proceeds by matching the two ingredients that define a sliced-Wasserstein discrepancy, namely (i) the slicing coordinate (projection map) and (ii) the slicing distribution on directions.

Step 1: The slicing coordinates coincide. The SPDSW construction [14] uses the matrix logarithm embedding

$$t^A(X) = \langle A, \log(X) \rangle_F, \quad A \in S_d(\mathbb{R}), \quad \|A\|_F = 1, \quad (146)$$

as its one-dimensional projection. In the present framework, the manifold is $\mathcal{M} = S_d^{++}$ and the pullback map is chosen as

$$\phi = \log : S_d^{++} \rightarrow S_d(\mathbb{R}). \quad (147)$$

Because the logarithm map satisfies $\log(I_d) = 0$, we choose the reference point as $x_0 = I_d$. The general PEM slicing coordinate given in Thm. 3.1

$$t_a(X) = \langle a, \phi(X) - \phi(x_0) \rangle_F = \langle a, \log(X) \rangle_F, \quad a \in S_{\mathcal{E}}, \quad (148)$$

where $\mathcal{E} = S_d(\mathbb{R})$ is equipped with the Frobenius inner product. Therefore, the PEM slicing coordinate t_a is exactly the SPDSW slicing coordinate t^A after identifying a .

Step 2: The slicing measures agree. The definition of PEMSW_p integrates over directions a drawn uniformly from the unit sphere

$$S_{\mathcal{E}} = \{a \in S_d(\mathbb{R}) : \|a\|_F = 1\}, \quad (149)$$

with respect to the uniform measure $\lambda_{\mathcal{E}}$. On the other hand, SPDSW samples symmetric directions through the spectral construction

described in [14], where one draws $P \in O_d$ from the Haar measure and $\theta \in S^{d-1}$ uniformly, and then sets $A = P \text{diag}(\theta) P^T$. Lemma 2.4 in [14] states that this procedure induces the uniform distribution on the unit Frobenius sphere of symmetric matrices, namely the same distribution as $\lambda_{\mathcal{E}}$ on $S_{\mathcal{E}}$.

Step 3: Equality of the discrepancies. Step 1 ensures that, for every direction, the corresponding one-dimensional pushforward measures coincide:

$$t_{a\#}\mu = t^A_{\#}\mu \quad \text{and} \quad t_{a\#}\nu = t^A_{\#}\nu, \quad (150)$$

whenever a and A represent the same point on the unit Frobenius sphere. Step 2 ensures that the integrations in the two definitions are taken with respect to the same distribution of directions. Consequently, the defining integrals match exactly:

$$\begin{aligned} \text{PEMSW}_p(\mu, \nu)^p &= \int_{S_{\mathcal{E}}} W_p^p(t_{a\#}\mu, t_{a\#}\nu) d\lambda_{\mathcal{E}}(a) \\ &= \int_{\|A\|_F=1} W_p^p(t^A_{\#}\mu, t^A_{\#}\nu) d\lambda_S(A) \\ &= \text{SPDSW}_p(\mu, \nu)^p. \end{aligned} \quad (151)$$

Taking the p -th root yields $\text{PEMSW}_p(\mu, \nu) = \text{SPDSW}_p(\mu, \nu)$.

This identity shows that SPDSW is recovered as a particular instance of the PEMS framework on S_d^{++} , where the global embedding map is the matrix logarithm and slicing is performed uniformly on the induced unit sphere of the embedding space. \square